

CHAPTER 6

Seismic Inversion Analysis Compared With Interpretation

In this chapter, a post-stack model-based deterministic inversion of the 3D Karewa dataset is described step by step. At first, seismic and well data are tied. An initial low-frequency model of acoustic impedance was created using a low-pass filter at the well location and extrapolating it to the whole zone of interest (H1 to H6). Then, a reflection coefficient model was made by deconvolving the seismic data using an extracted wavelet. The absolute acoustic impedance model was derived from constrained deterministic inversion by using relative acoustic-impedance inversion and the initial model. Finally, the inversion process was applied to the seismic data cube from 800 ms to 2500 ms. Hampson-Russell software was used for the whole inversion analysis.

6.1 Seismic to Well Tie

One of the most important tasks for inversion analysis is to tie the seismic and well data for time-depth conversion. Seismic data is in time domain and well logs are in depth domain. As in this study the check shot data is not available, an ‘adaptive approach’ is applied for seismic-to-well tie (Simm and Bacon, 2014). At first, the amplitude spectrum is estimated and the equivalent wavelet (180° phase) is derived from the seismic data as the seismic data has European polarity. Then sonic log integration is used for depth-to-time conversion. A synthetic seismogram is generated to cross-correlate with the seismic trace. A bulk shift is applied to correlate the synthetic to the seismic data and the shape of the cross-correlation function is evaluated to keep the cross-correlation function symmetrical by rotating the wavelet phase. A wavelet is then extracted from the well for the cross-correlation to estimate the best-correlating wavelet.

A statistical wavelet with an assumed phase (matching the nominal seismic data phase) was extracted from the seismic data (Figure 6-1). The wavelet length was 200 ms

and the extracted trace was from inline 1177 and crossline 3980. The wavelet was assigned 180° phase as the seismic data polarity is negative (European polarity), based on the sea-floor reflection. The taper length was 25 ms and constant phase type is used. The target time window was constrained by H1 and H6.

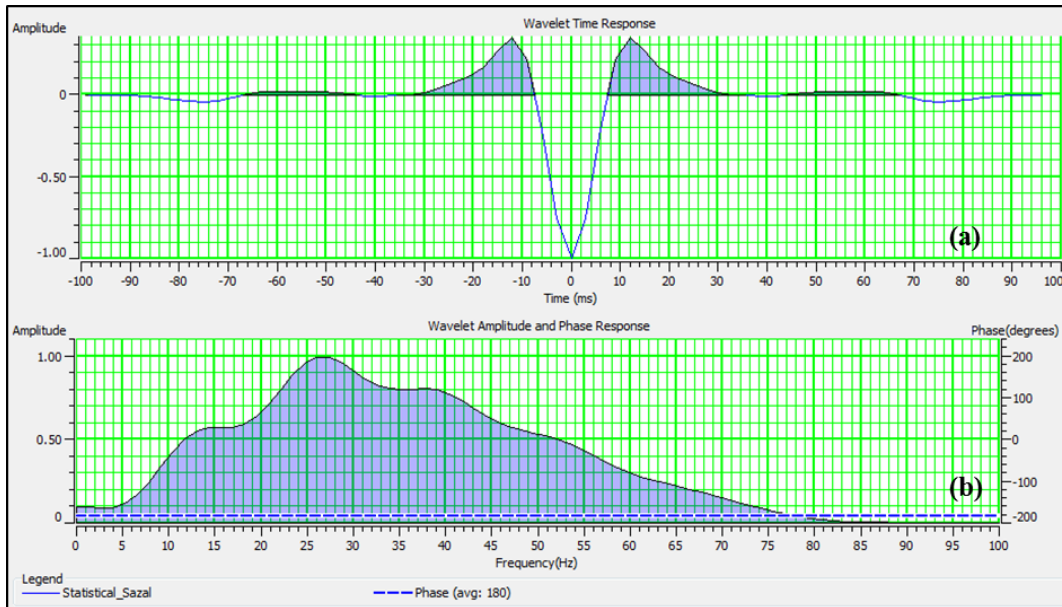


Figure 6-1: The extracted statistical wavelet assigned the nominal phase of seismic data. The wavelet length is 200 ms, taper length is 25 ms, and phase is 180° . (a) wavelet in time domain, (b) wavelet in frequency domain: amplitude and phase spectra.

The Karewa-1 well logs and seismic data were tied using Hampson-Russell software. Sonic log integration was used for depth to time conversion. The correlation of well logs and seismic data is important to validate the horizons and also help to estimate the actual phase of seismic data.

The well was tied to the seismic data and a statistical wavelet was extracted (Figure 6-2). The synthetic traces (blue) are calculated from the sonic and density logs of Karewa-1 well and the extracted statistical wavelet. The composite traces (red) are extracted from the seismic traces (black). The cross-correlation window was 1300 ms to 1900 ms and the maximum cross-correlation equaled 0.74, found at time shift of 3 ms down. In this case the cross-correlation function is not symmetrical. Phase rotation is therefore required along with a time shift to get the proper wavelet extraction from the seismic data.

The phase was rotated -38° to match the phase of the seismic data. Then a second seismic-to-well tie was applied using this wavelet (Figure 6-3). The cross-correlation window was 1300 ms to 1900 ms and the maximum cross-correlation was 0.76, with a time shift of -2 ms down. This wavelet is shown in Figure 6-4.

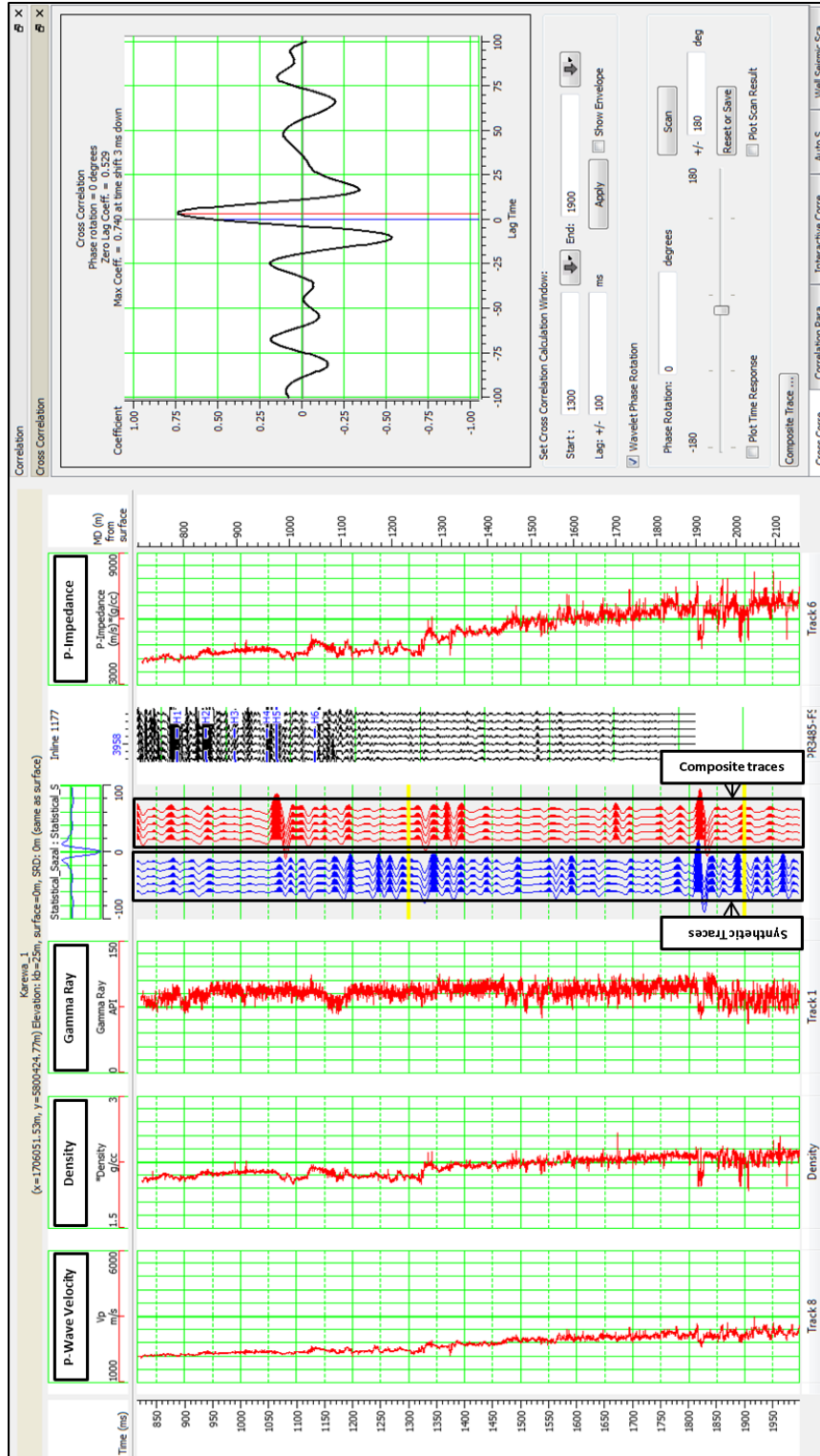


Figure 6-2: Seismic-to-well tie using the extracted statistical wavelet (180° phase) with maximum cross-correlation of 0.74 over the interval 1300-1900 ms. The composite traces are the real seismic traces that follow the time (TWT) scale in ms. The traces shown in inline 1177 column are seismic traces that do not follow the time (TWT) in ms.

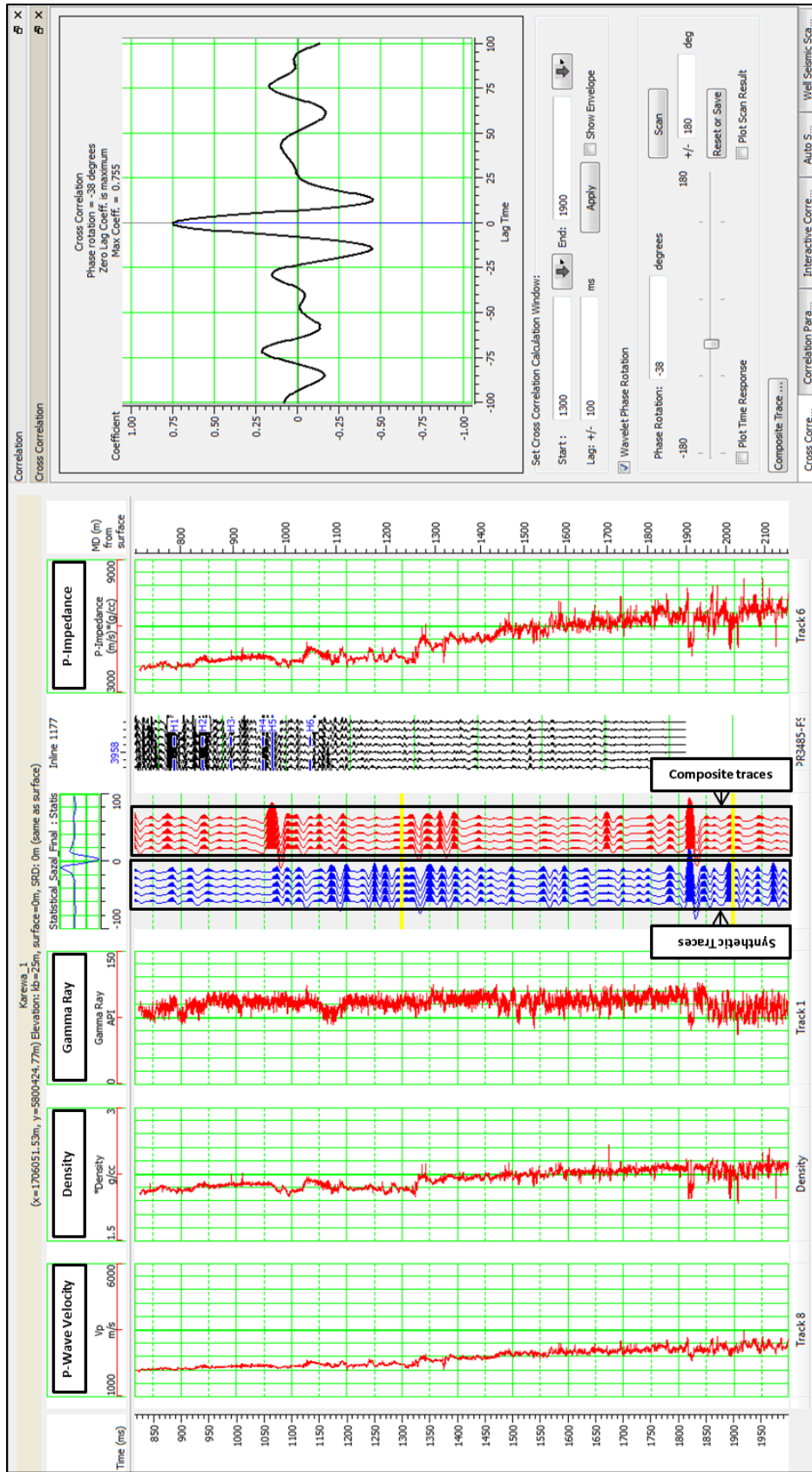


Figure 6-3: Seismic-to-well tie using the corrected wavelet from seismic data (142° phase) with maximum cross-correlation equal to 0.76 with a -2ms time shift measured over the interval 1300-1900 ms. The composite traces are the real seismic traces that follow the time (TWT) scale in ms. The traces shown in inline 1177 column are seismic traces that do not

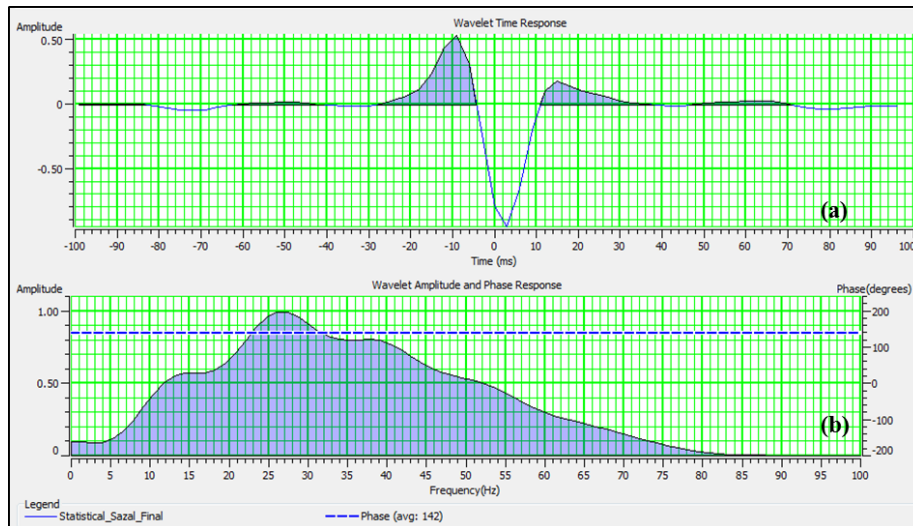


Figure 6-4: The phase-corrected wavelet extracted from seismic data. The wavelet length is 200 ms, taper length is 25 ms, and phase 142° . (a) wavelet in time domain, (b) wavelet in frequency domain: amplitude and phase spectra.

A wavelet is also extracted from the Karewa-1 well (Figure 6-5). The wavelet length was 200 ms and trace extracted from inline 1177 and crossline 2800-4800. The taper length equals 25 ms. Neighborhood radius equal to 5 is used to calculate composite trace. The reflectivity spectrum was smoothed with a 10Hz low-pass filter. The target window was constrained by H1 and H6.

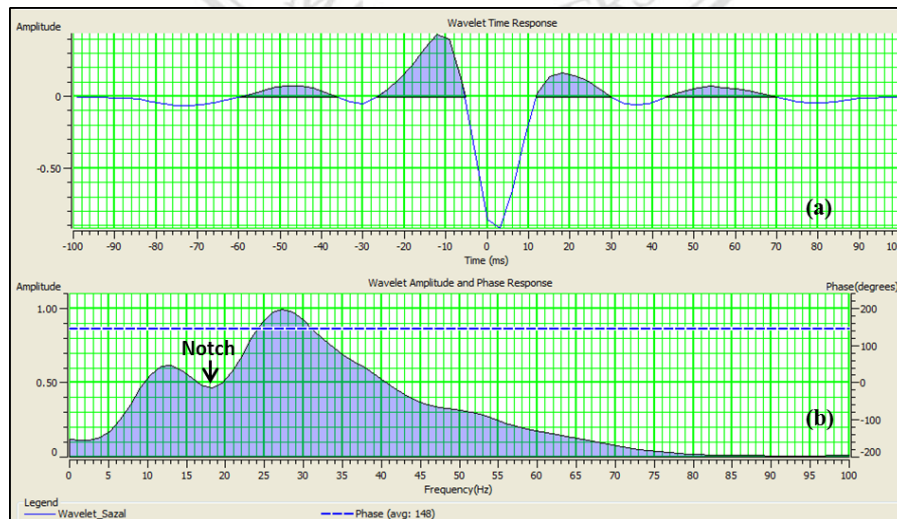


Figure 6-5: Extracted wavelet from well tie using logs. The wavelet length is 200 ms, taper length is 25 ms, and phase 148° . (a) wavelet in time domain, (b) wavelet in frequency domain: amplitude and phase spectra.

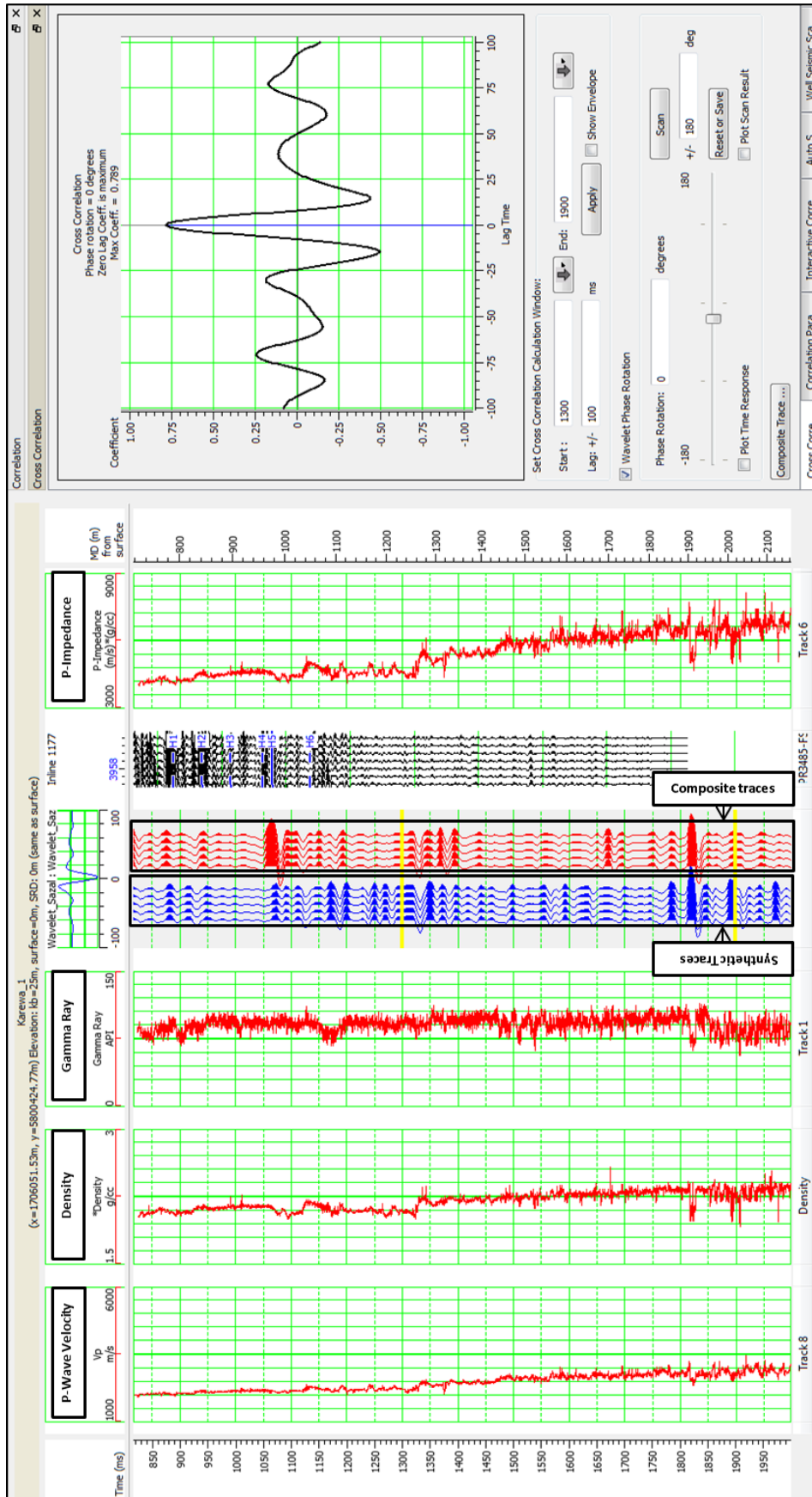


Figure 6-6: Seismic-to-well tie using the wavelet extracted from the Karewa-1 well tie using logs (148° phase) with maximum cross-correlation equal to 0.79 with a 1 ms time shift measured over 1300–1900 ms. The composite traces are the real seismic traces that follow the time (TWT) scale in ms. The traces shown in inline 1177 column are seismic traces that do not follow the time (TWT) in ms.

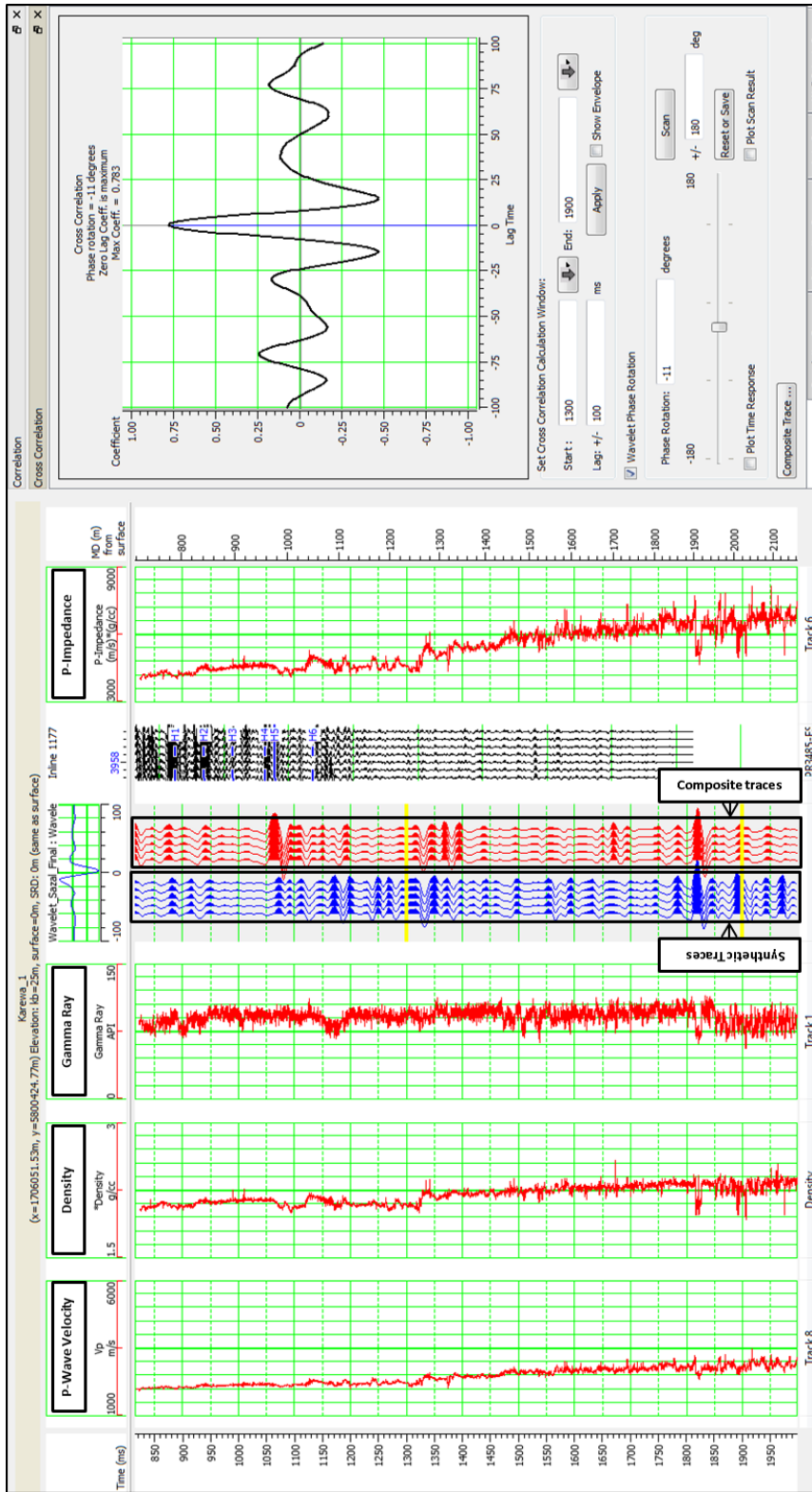


Figure 6-7: Seismic-to-well tie using the wavelet extracted from well logs (phase-rotated to 137°) with maximum cross-correlation equal to 0.78 with a 1 ms time shift, measured over 1300-1900 ms. The traces shown in inline 1177 column are seismic traces that do not follow the time (TWT) in ms. In a third seismic-to-well tie, the wavelet was extracted from the well tie (Figure 6-6). The cross-correlation window was 1300 ms to 1900 ms and the maximum correlation value equal to 0.79 was found at 1 ms time shift. In this case the cross-correlation function is not symmetrical. Phase rotation is therefore required with the time shift to get the proper wavelet extraction from the well logs.

The phase is rotated -11° to get the new wavelet from the well tie using logs. The fourth seismic-to-well tie was done using this wavelet (Figure 6-7). The cross-correlation window was 1300 ms to 1900 ms and maximum correlation value equal to 0.78 is found at time shift of 1 ms down. This wavelet is shown in Figure 6-8.

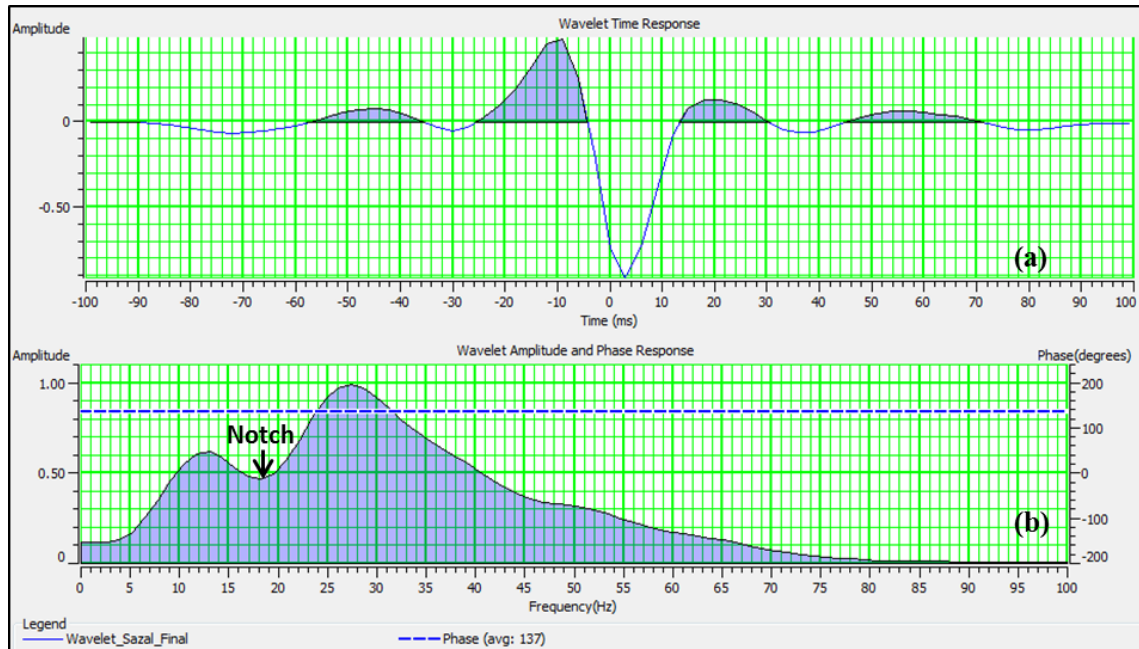


Figure 6-8: Wavelet extracted from the well tie using logs, rotated for the best cross-correlation. The wavelet length is 200 ms, taper length is 25 ms, and phase 137° . (a) wavelet in time domain, (b) wavelet in frequency domain: amplitude and phase spectra.

So far four seismic-to-well ties were applied. The second tie used the wavelet extracted from autocorrelation of the seismic data and the fourth tie used the wavelet extracted from the well tie using logs. Between these two phase-rotated wavelets, the wavelet from the well tie has a better cross-correlation although the amplitude spectrum of this wavelet from well shows a notch which can eliminate frequencies or boost noise at the frequency component. Thus the phase-rotated extracted wavelet from the seismic data was chosen for the final seismic-to-well tie and further inversion analysis. The time-depth curve from the seismic-to-well tie is shown in Figure 6-9.

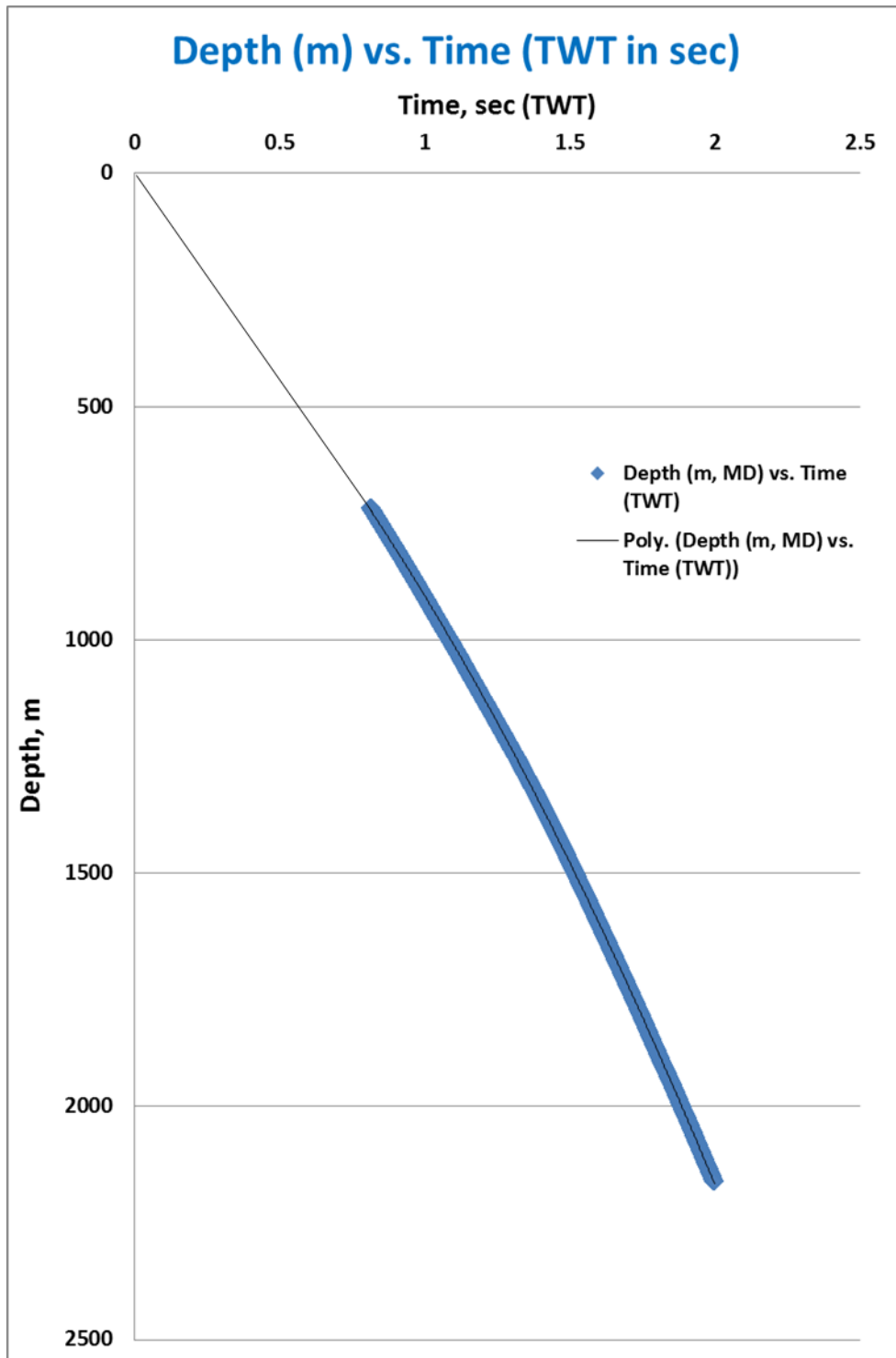


Figure 6-9: The time-depth curve from the seismic-to-well tie.

6.2 Building Low Frequency Initial Model

The low-frequency initial model contains well or other information with frequencies lower than those contained in the seismic data. The objective of building this model is to model properties in frequencies lower than those contained in the seismic data. The initial model is built by using the well data constrained by the picked horizons. The original acoustic impedance is calculated from the well data. Later picked horizons are used to guide the interpolation of acoustic impedance that is calculated from the well log. A low-pass filter is used to extract resulting acoustic impedance values to frequencies less than the frequencies found in the seismic data.

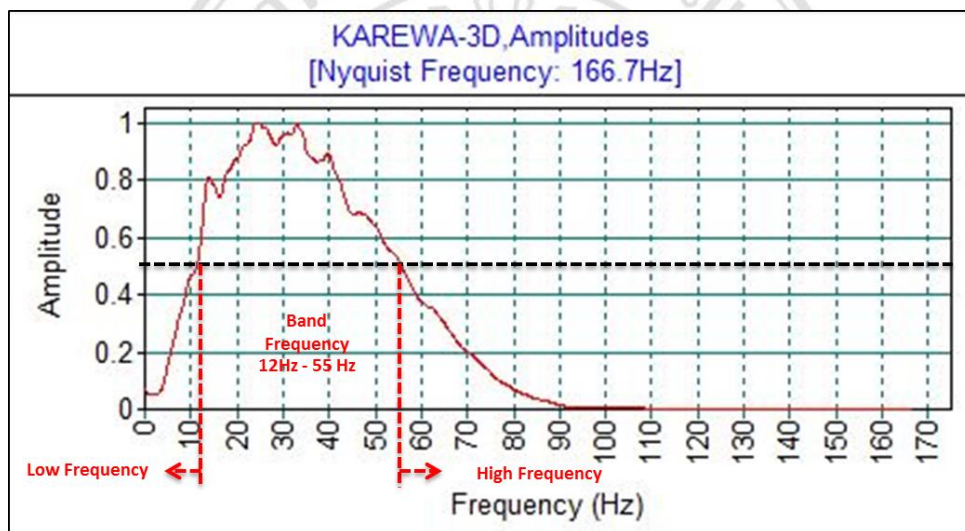


Figure 6-10: Amplitude spectrum analysis of 3D Karewa dataset

The bandwidth of 3D Karewa seismic data ranges from 12 to 55 Hz (Figure 6-10). The Nyquist frequency of the data is 167 Hz and the mean frequency of the seismic energy is around 30 Hz. The overall data frequency content is good but the seismic data cannot be observed below 12 Hz. The average velocity until the top of the reservoir sand is 2480 m/s in seismic data. The average velocity is 2540 m/s and the dominant frequency in the reservoir sand is 37 Hz (Figure 6-11). The tuning thickness is 20 meter. The thickness of the Mangaa C-1 sand is 12 m (Conoco Northland Ltd., 2002-2003). The low frequency model is established to get the seismic data less than 12 Hz frequency.

To build the low frequency initial acoustic impedance (P-impedance) model, user defined parameters are set. The impedance logs are calculated using the corrected p-wave, and density logs after the seismic-well tie. The post-stack model type was used in the Hampson-Russell software. Karewa-1 well logs were taken from the database of project database of the software. 3D Karewa seismic data is used as the reference grid. Three different bandpass filters are applied to the seismic data with the 800-2500 ms time (TWT) interval. In Figure 6-12, few seismic reflections can be observed for bandpass filter (0-0-10-15 Hz) and no seismic reflections can be observed less than this filter in TWT interval from 800-2500 ms. To build the low frequency initial model a low pass filter (10/15 Hz) was applied where 10 Hz is the high-cut filter frequency and 15 is the taper frequency. The time window was selected from 800 ms to 2500 ms. Figure 6-13 shows the low frequency p-impedance initial model. As for the low frequency acoustic impedance initial model, initial models for density and p-wave were also created using the same parameters but density and p-wave logs are used instead of p-impedance log. The Hampson-Russell software creates the low frequency initial model for density and p-wave simultaneously with p-impedance. Figure 6-14 and Figure 6-15 show the initial models for density and p-wave respectively.

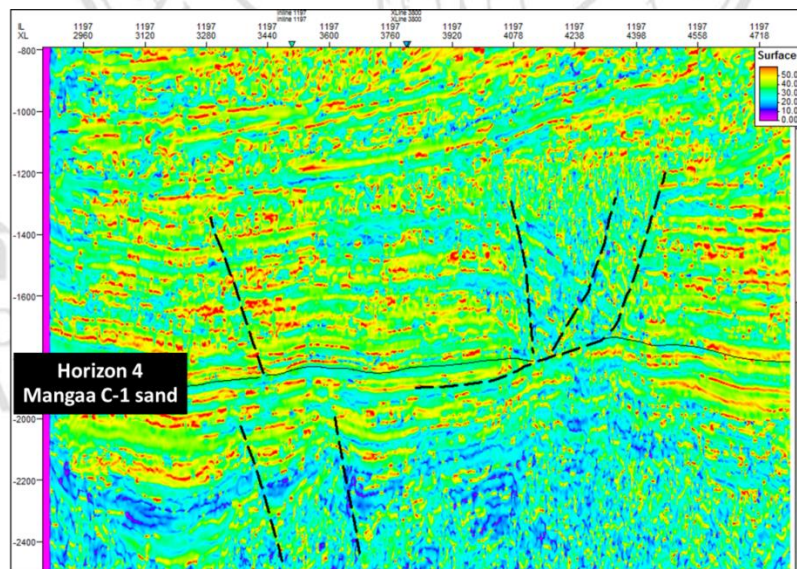


Figure 6-11: Dominant frequency attribute shows H-4 (Mangaa C-1) which has 37 Hz dominant frequency in inline 1177. The scale bar shows the dominant frequency ranging from 0 to 60 Hz.

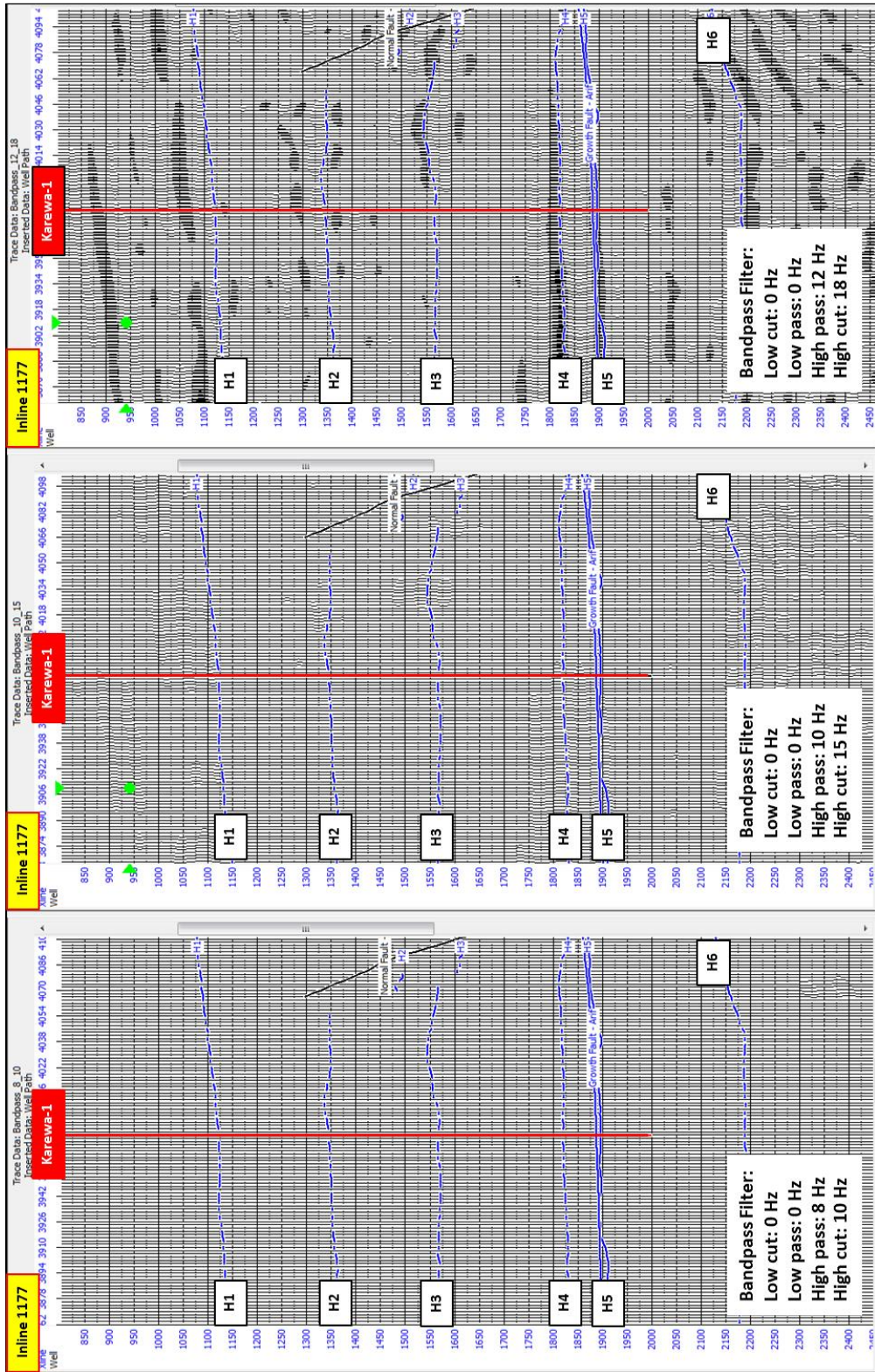


Figure 6-12: Outputs after applying three different filters to the seismic data between time interval 800 and 2500 ms.

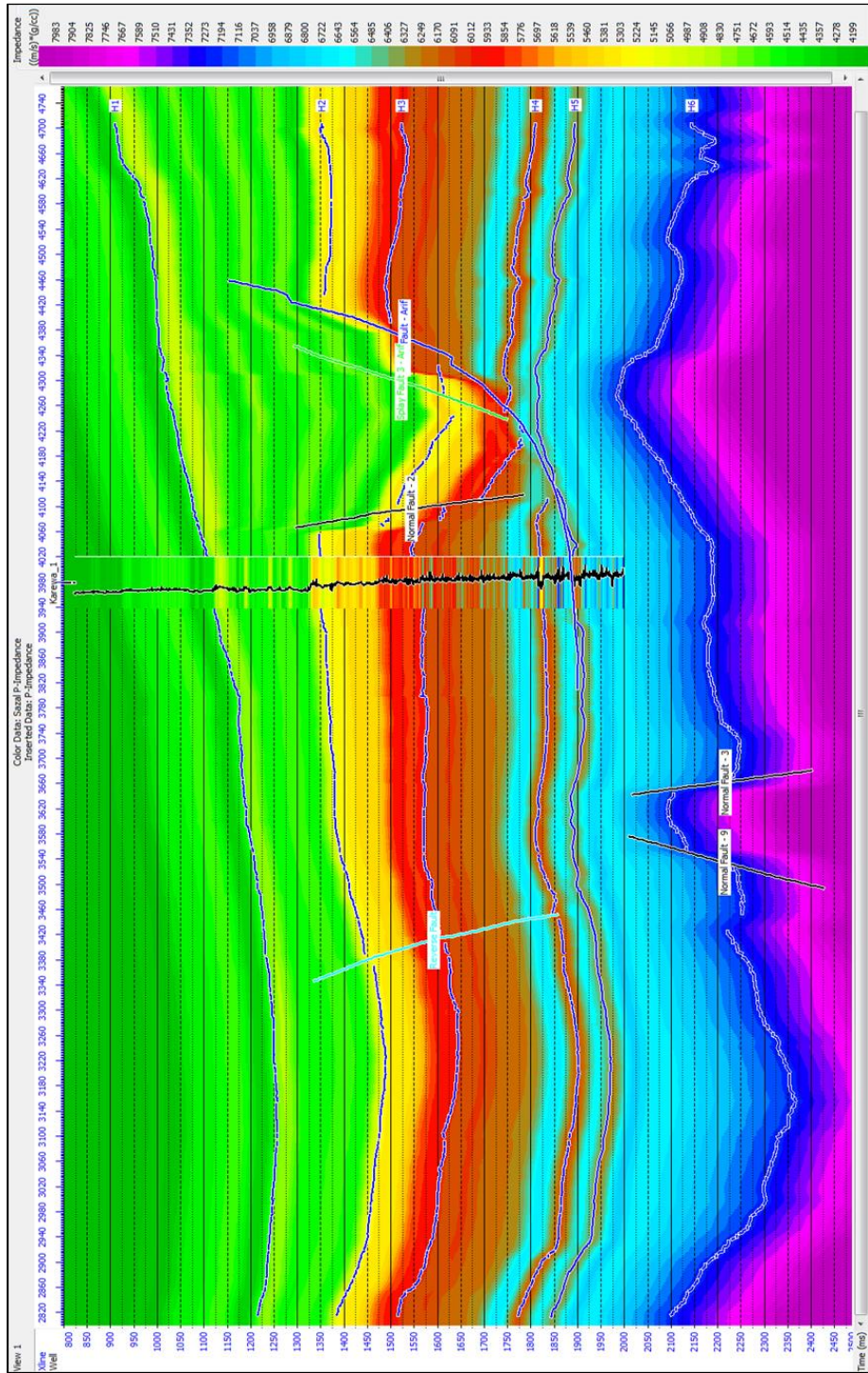


Figure 6-13: The low frequency initial P-impedance model at inline 1177. The p-impedance log in colour ribbon almost matches the initial model. The p-impedance log is also shown as a black line inside the colour ribbon. The colour bar illustrates p-impedance values in $(\text{m/s}) * (\text{g/cc})$.

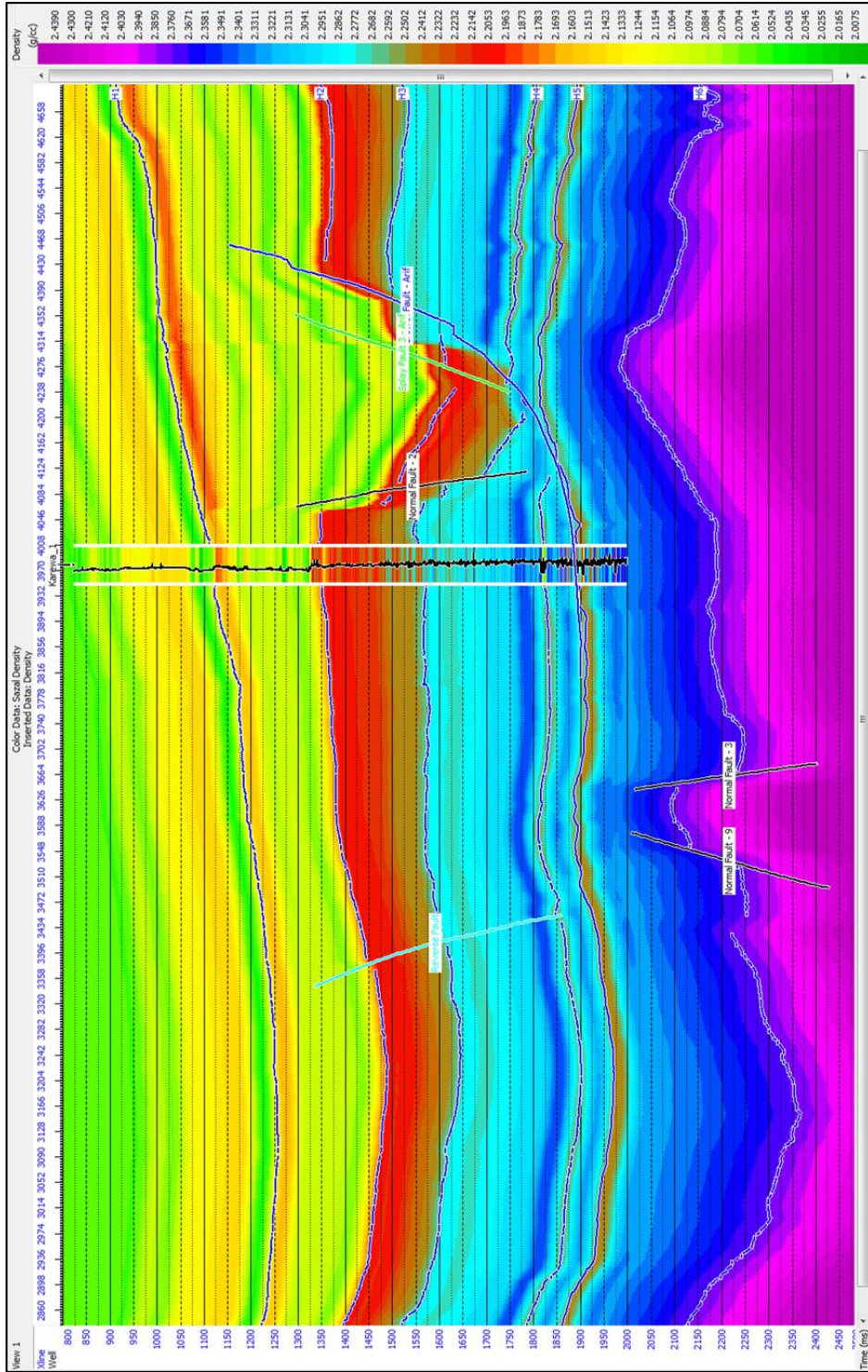


Figure 6-14: The initial low frequency density model at inline 1177. The density log in colour ribbon almost matches the initial model. The density log is also shown as a black line inside the colour ribbon. The colour bar illustrates density values in (g/cc).

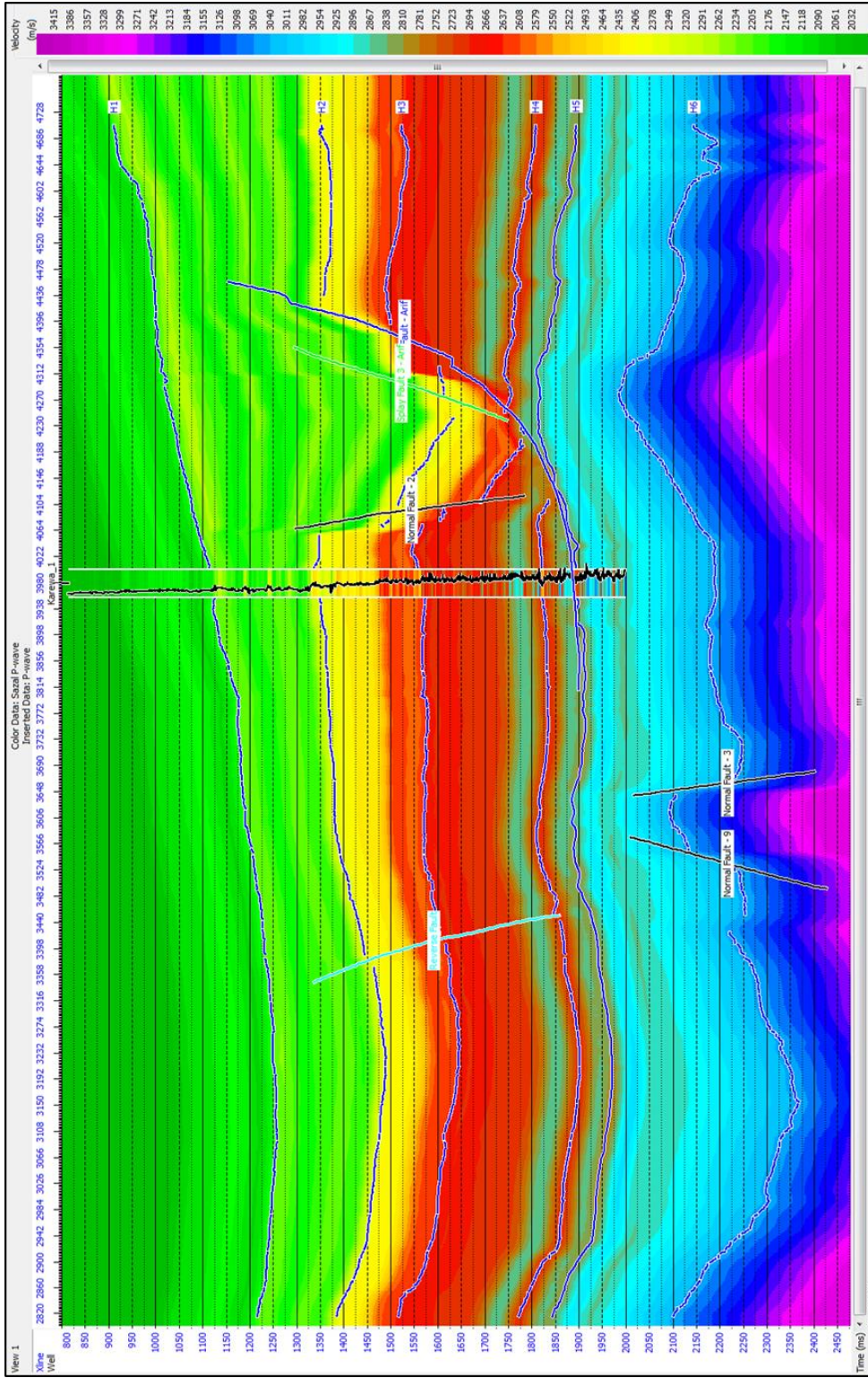


Figure 6-15: The initial low frequency p-wave model at inline 1177. The p-wave log in colour ribbon almost matches the initial model. The p-wave log is also shown as a black line inside the colour ribbon. The colour bar illustrates p-wave values in (m/s).

6.3 Model-based Deterministic Inversion Analysis

In this workstep, the model-based deterministic inversion is applied. The hard-constraint option was used which sets the maximum allowable deviations (up and down) in impedance as a percentage of the average impedance of the constraint log. In this case 100% upper and lower percentage limits are taken because if these percentages are reduced, the constraint would be tightened. The average block size was 3 ms, which sets the thickness in milliseconds for the initial equal travel-time layers of the model. Prewhitening was set to 1% as a default in Hampson-Russell software although it is the noise level that is added to the amplitude spectrum of the data before analysis. The best result comes without prewhitening but sometimes it is needed to set to stabilize the operation. The number of iterations was set to 20 to improve the convergence. The phase-rotated wavelet (phase 142°) extracted from the seismic data was chosen for the inversion analysis. In Figure 6-16, the amplitude spectrum is not so similar for the time interval 800-1400 ms and 1900-2500 ms. However, the inversion is applied between 800 ms and 2500 ms. The reason behind this is the difficulty to make initial models by separating the zones based on time interval as all horizons have common time (TWT) in different places in this study. This phenomenon specially occurred in H-2, H-3, and H-4 due to the big faults (Karewa Fault and N. Fault 10).

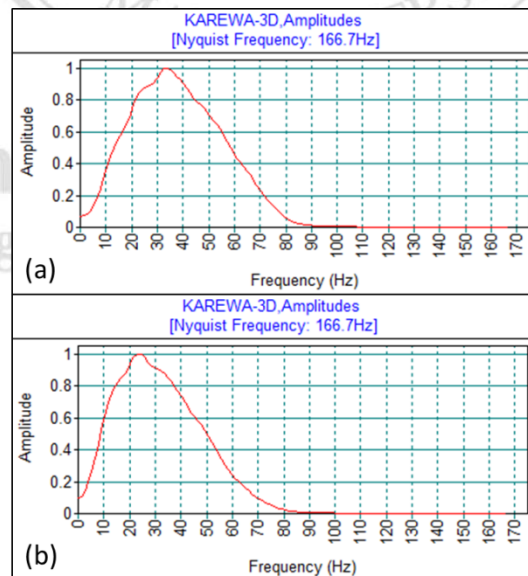


Figure 6-16: Amplitude spectrum between the time interval (a) 800-1400 ms, and (b) 1900-2500 ms

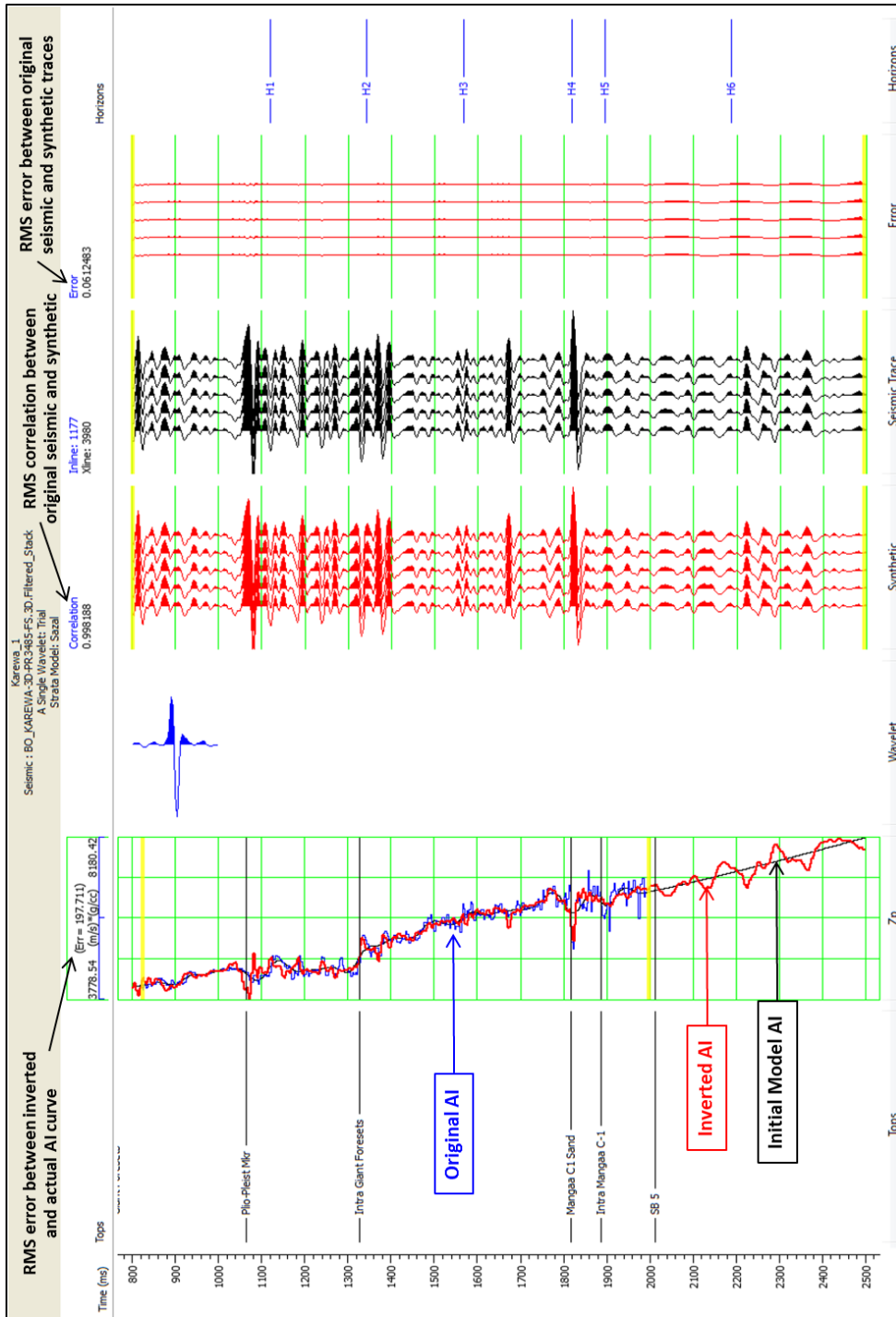


Figure 6-17: The acoustic impedance inversion (correlation and error) analysis using phase rotated wavelet (142° phase) extracted from seismic data.

Figure 6-17 shows the acoustic impedance inversion analysis using the phase rotated wavelet (142° degree phase) extracted from seismic data. Three curves are shown in the Z_p column and they have same trend. The blue curve shows the original acoustic impedance (AI) calculated from log whereas the red and black curves show the inverted and initial model acoustic impedance (AI) respectively. The Z_p column ranges 3779-8180 ((m/s)*(g/cc)). The error value shown in the above of the Z_p column expresses the RMS error between inverted and actual acoustic impedance (AI) curves. The synthetic traces are calculated using logs and wavelet. Error traces are calculated by subtracting the synthetic traces from the original seismic traces. These traces show the difference between synthetic and original seismic traces in graphical form. The value shown in the above of the synthetic trace column expresses the RMS correlation between original and synthetic traces and the value shown in the above of the error trace column expresses the RMS error between original and synthetic traces. Figure 6-18 shows a linear relationship between inverted and original acoustic impedance (AI) logs. The values of acoustic impedances of original, inverted, and initial model are reasonable. The inversion result seems correct.

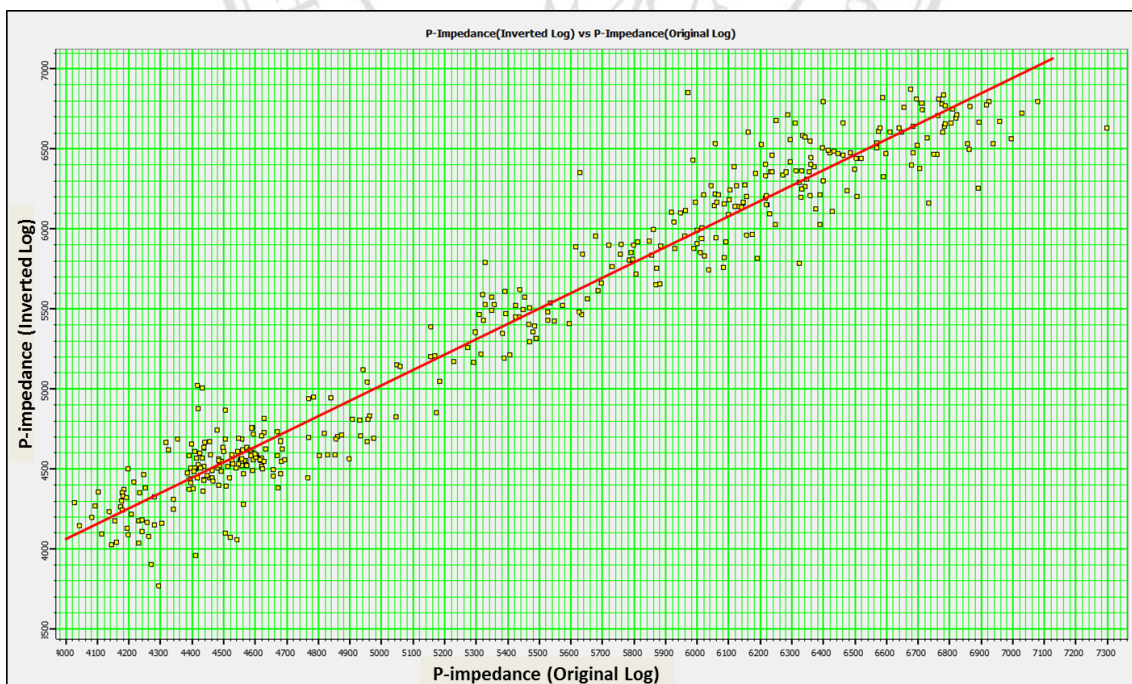


Figure 6-18: Inverted vs. Original P-Impedance log plot shows a linear relationship

6.4 Inversion Results

The post-stack model-based deterministic inversion was applied to the 3D Karewa seismic data between 800 ms and 2500 ms. The target zone for inversion analysis (H1 to H6) is located in this time interval. Reflection series were extracted from the seismic data by deconvolving the seismic data and then the acoustic impedance from the reflection series is extracted by the Hampson-Russell software throughout the data volume constrained by the time interval. The Hampson-Russell software can also extract the inverted density and p-wave volume by taking the correlation of density and p-wave logs with acoustic impedance log using the low frequency initial models of density and p-wave.

Figure 6-19 shows the acoustic impedance (AI) distribution from model-based deterministic inversion at inline 1177 where the Karewa-1 well is located. The acoustic impedance (AI) log is shown in colour ribbon that matches with the impedance distribution quite well. The colour bar illustrates inverted acoustic impedance values ranging from 4100 to 8000 ((m/s)*(g/cc)) at inline 1177. A gamma ray log is also shown inside the colour ribbon to identify the sand and shale/clay. From a quick look it can be observed that low acoustic impedance values are mostly in shallow depth and values increase with depth because of compaction effects. The inversion result shows that zones with low gamma ray values have low acoustic impedance and vice versa. The high gamma ray values indicate non-permeable rocks such as shale or clay, and low gamma ray values indicate permeable rock such as sand.

Figure 6-20 shows the distribution of acoustic impedance, density, and p-wave velocity from at inline 1177. As same as the acoustic impedance distribution, shallow zones have lower values of density and p-wave. Colour bars illustrate inverted volume values. The p-wave velocity ranges from 2000 (m/s) to 3460 (m/s) and the density ranges from 2.0055 (g/cc) to 2.44 (g/cc). Their values increase with depth for compaction effect. The colour ribbons show the original logs associated with every inverted volume. The original logs (ribbons) match very well with the associated inverted volume. Gamma ray logs are shown inside the colour ribbons to identify the sand and shale/clay. Typically, zones containing low acoustic impedance have low density and vice versa. The low values of acoustic impedance, p-wave, and density can

be found in deeper zone if that zone is fluid saturated. For instance in Figure 6-20, H-4 has low values of acoustic impedance, p-wave velocity, and density and H-4 is located between zones that have high acoustic impedance, p-wave velocity, and density.

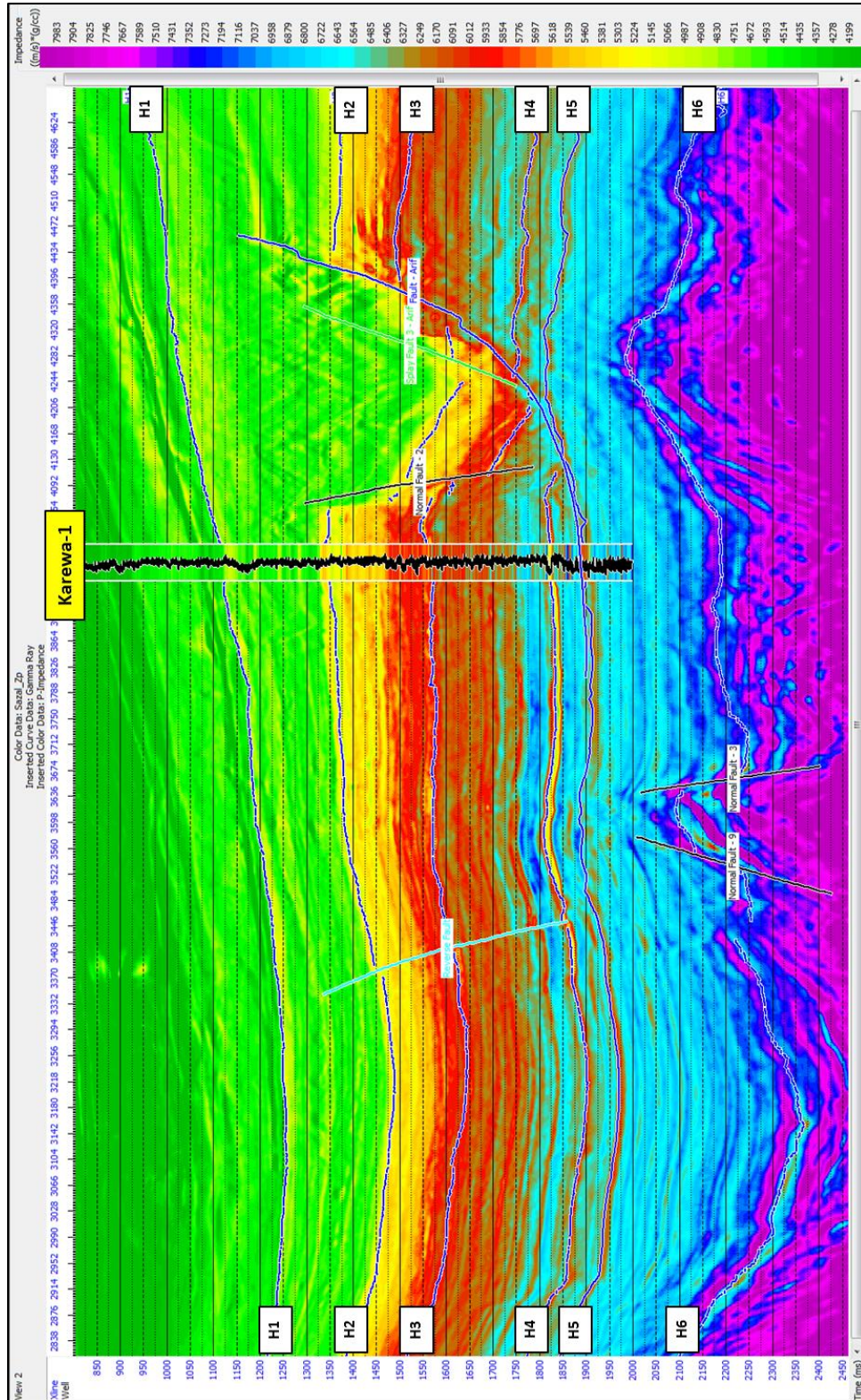


Figure 6-19: The acoustic impedance (AD) distribution from model-based deterministic inversion at inline 1177. The acoustic impedance (AD) log in colour ribbon matches with the impedance distribution. A gamma ray log is also shown inside the colour ribbon. The colour bar illustrates acoustic impedance values in $(\text{m/s}) \cdot (\text{g/cc})$.

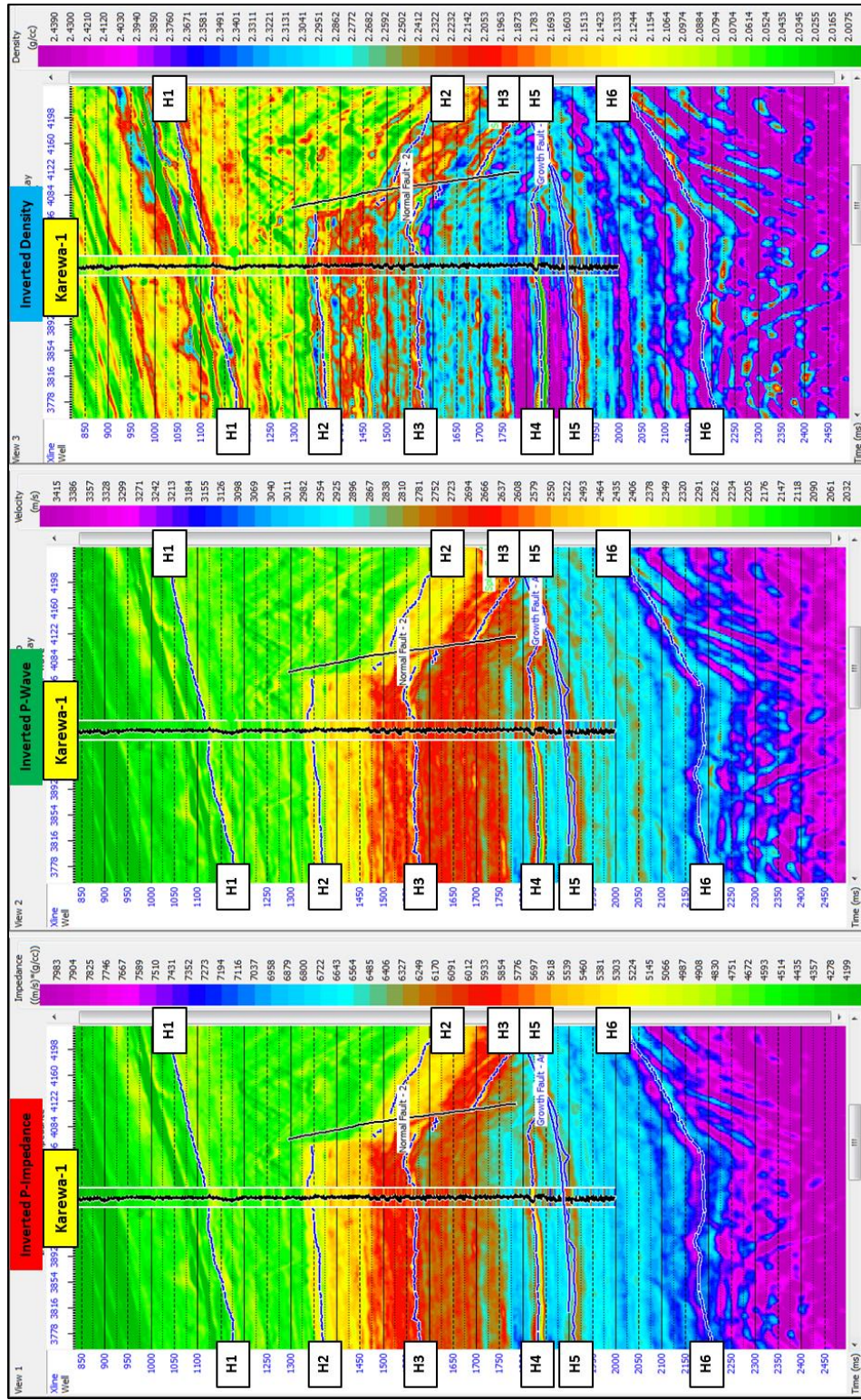


Figure 6-20: The distribution of acoustic impedance, density, and p-wave from model-based deterministic inversion at inline 1177. The colour ribbons show the original logs associated with those inverted volumes. The ribbons match with the associated inverted volume distribution. A gamma ray log is also shown inside each colour ribbon.

6.5 Combination of Inversion Results with Interpretation and Attributes

H-1 (Plio-Pleist Mkr + 39ms TWT at the Karewa-1 well location in inline 1178) was interpreted on a high negative amplitude reflection (trough) of high to medium continuity (section 5.1). The acoustic impedance distribution map of H-1 (Figure 6-21) shows that H-1 has low acoustic impedance ranges from 4200 to 4900 throughout the surface except in the middle. Some small areas of the center have comparatively medium acoustic impedances ranging from 5200 to 5500 ((m/s)*(g/cc)). This difference can be occurred due to the lithology variation during deposition process as H-1 dripping from ESE to WNW (section 5.1). The acoustic impedance values are comparatively very low in the ESW and WNW. It can be due to acquisition or processing error because the seismic reflections are dim in these zones (Figure 6-22).

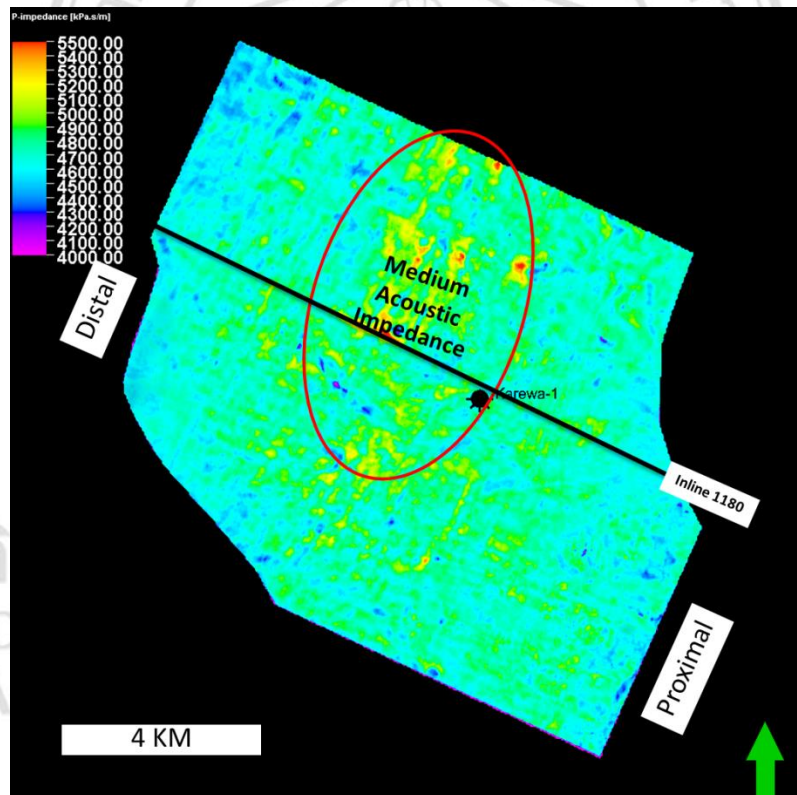


Figure 6-21: The distribution of acoustic impedance on H-1 surface. Search window (below or above H-1) was zero ms TWT. The green arrow indicates the north direction.

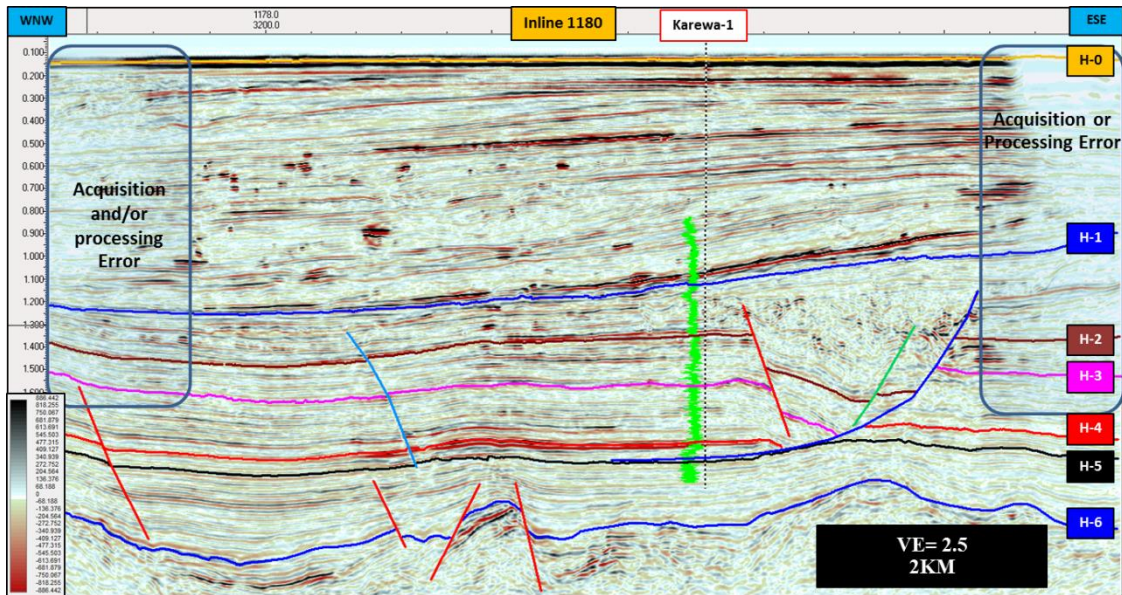


Figure 6-22: Inline 1180 shows the probable acquisition or processing error in the WNW and ESE.

H-2 (Intra Giant Foresets + 15ms TWT at the Karewa-1 well location in inline 1178) was interpreted on a medium positive amplitude reflection (peak) of low to medium continuity (section 5.1). The acoustic impedance distribution map of H-2 (Figure 6-23) ranges from 4900 to 5700 ((m/s)*(g/cc)) and shows that H-2 has low to medium acoustic impedance in most of its area except in the NW, and the east. In the NW and east there is comparatively low acoustic impedance ranging from 4900 to 5100 ((m/s)*(g/cc)). This difference can be occurred due to the lithology variation, acquisition or processing error (Figure 6-22), and/or mispick of the horizon due to low continuity as there are low amplitude reflections.

In Figure 6-23, low to medium acoustic impedance distribution can be observed and these low acoustic impedance zones seems like channels although the most positive 3D curvature attribute map of H-2 (Figure 6-24) shows no channel shape and RMS amplitude attribute map of H-2 (Figure 6-25) shows the amplitude variations as same as acoustic impedance variation map (Figure 6-23). So the acoustic impedance variation in the middle is likely the result of the lithology change.

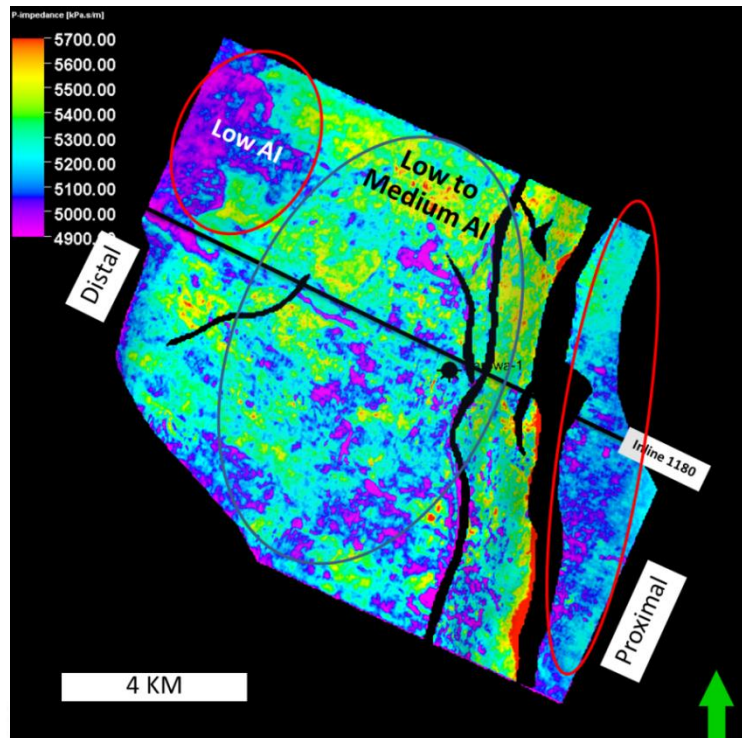


Figure 6-23: The distribution of acoustic impedance on H-2 surface. Search window (below or above H-2) was zero ms TWT. The green arrow indicates the north direction.

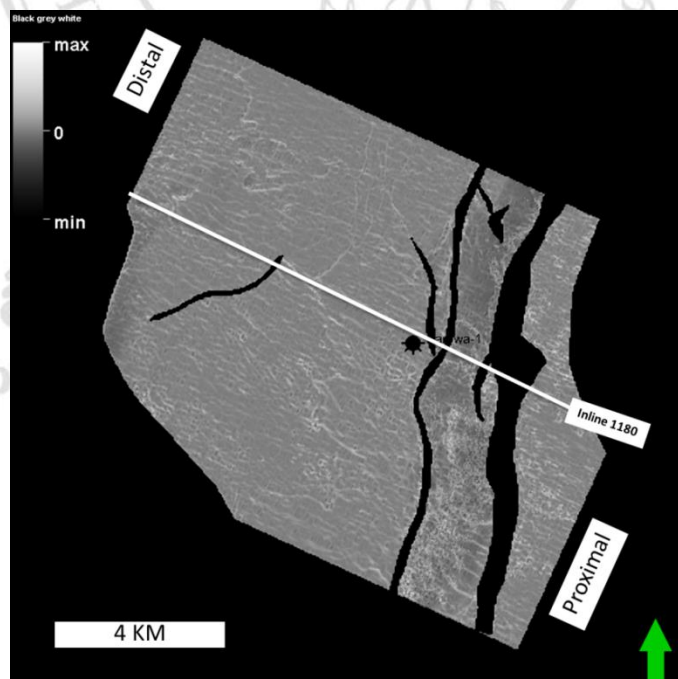


Figure 6-24: Most positive 3D curvature attribute map of H-2. Search window (below or above H-2) was zero ms TWT. The green arrow indicates the north direction.

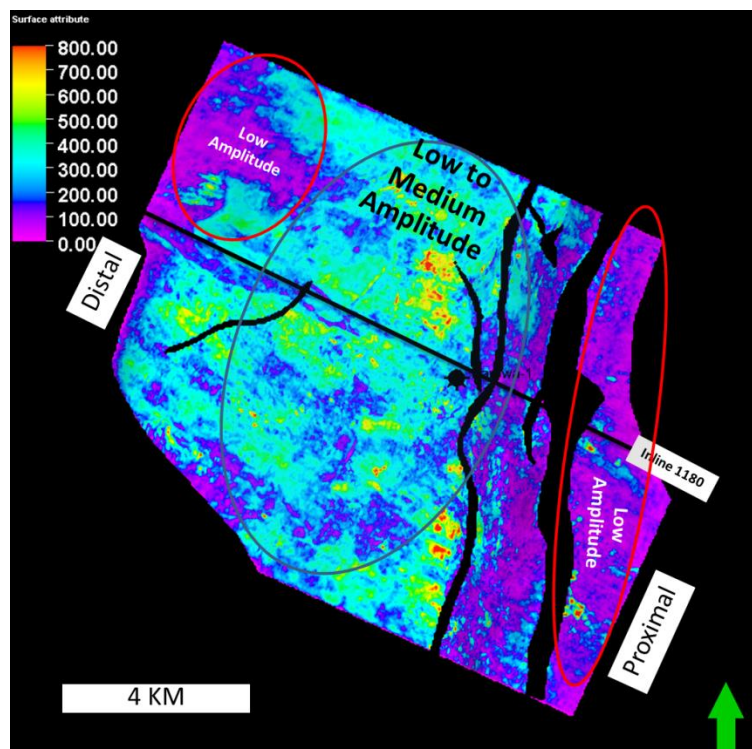


Figure 6-25: RMS amplitude attribute map of H-2. Search window (below or above H-2) was zero ms TWT. The green arrow indicates the north direction.

H-3 (1571ms TWT at the Karewa-1 well location in inline 1178) was interpreted on a positive amplitude reflection (peak) of medium to low continuity (section 5.1). The acoustic impedance distribution map of H-3 (Figure 6-26) ranges from 5100 to 6200 ((m/s)*(g/cc)) and shows that H-3 has medium range of acoustic impedance in most of its area except in the center near big faults. In this zone there is comparatively low to medium acoustic impedance ranging from 5100 to 5500 ((m/s)*(g/cc)). This difference can be occurred due to the lithology variation, fluid effect, and/or mispick of the horizon due to low continuity as there are low amplitude reflections.

In Figure 6-27, the RMS amplitude and envelope attribute map of H-3 shows the high RMS amplitude and high envelope values at the same zone whereas the acoustic impedance distribution map shows low acoustic impedance. High values of RMS amplitude and envelope means the high contrast of acoustic impedance. So this zone might be affected by the fluid content.

The sweetness distribution map of H-3 is shown in Figure 6-28. Sweetness is actually a combined implementation of envelope and instantaneous frequency attributes

which identifies the overall energy signatures change in the seismic data. Figure 6-28 shows the high sweetness values at the same zone whereas the RMS amplitude and envelope map showed high values.

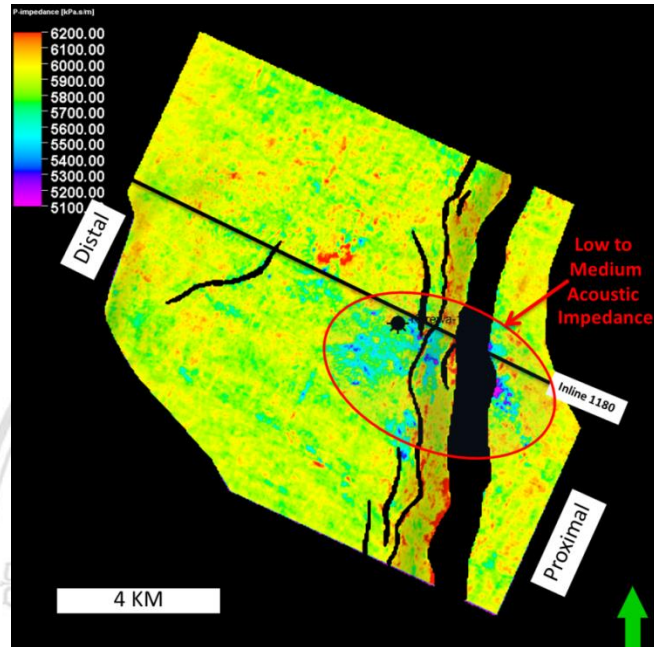


Figure 6-26: The distribution of acoustic impedance on H-3 surface. Search window (below or above H-3) was zero ms TWT. The green arrow indicates the north direction.

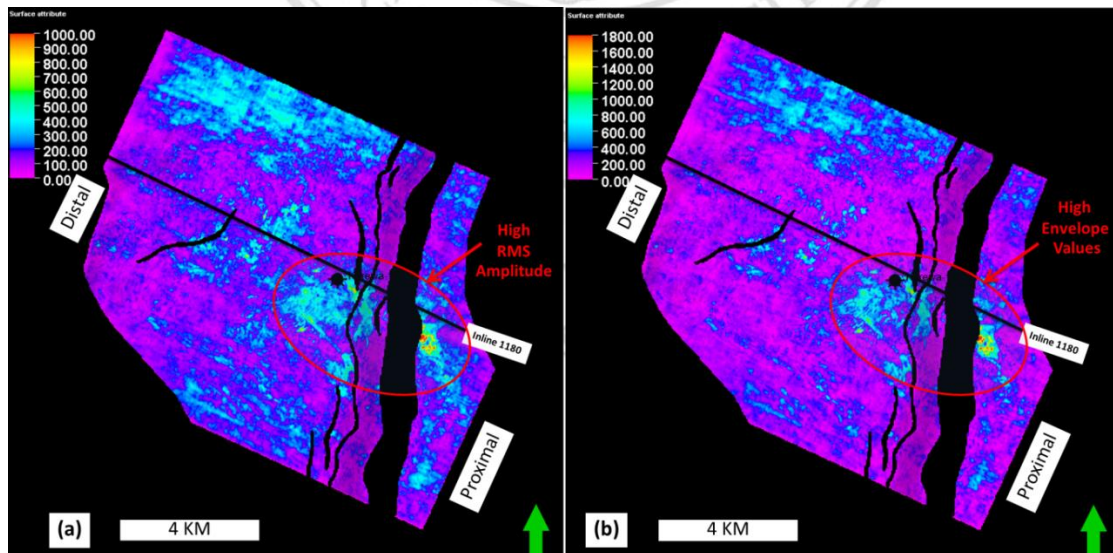


Figure 6-27: (a) RMS amplitude attribute map of H-3, and (b) Envelope attribute map of H-3. Search window (below or above H-3) was zero ms TWT. The green arrow indicates the north direction.

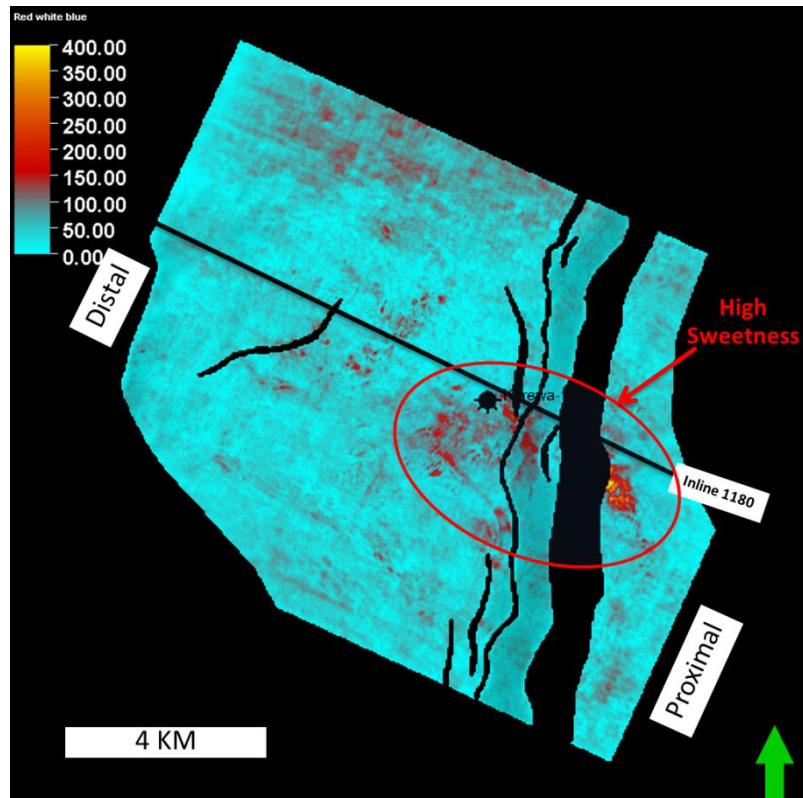


Figure 6-28: Sweetness attribute map of H-3. Search window (below or above H-3) was zero ms TWT. The green arrow indicates the north direction.

H-4 (top of Mangaa C-1 Sand) was interpreted on a prominent positive amplitude reflection (peak) of high to medium continuity (section 5.1). The acoustic impedance distribution map of H-4 (Figure 6-29) ranges from 4600 to 7000 $((m/s)*(g/cc))$ and shows that H-4 has medium to high range of acoustic impedance in most of its area except in the central area. In this zone there is low acoustic impedance ranging from 4600 to 5500 $((m/s)*(g/cc))$. The time structure map contour on Figure 6-29 represents the high structure. This zone is gas saturated Mangaa C-1 Sand.

In Figure 6-30, the RMS amplitude and envelope attribute map of H-4 shows the high RMS amplitude and high envelope values at the high structure zone with very low acoustic impedance. High values of RMS amplitude and envelope means the high contrast of acoustic impedance. So this horizon is hydrocarbon bearing.

The sweetness attribute map of H-4 in Figure 6-31 shows the high sweetness values at the high structure where high values of RMS amplitude and envelope is found with low values of acoustic impedance.

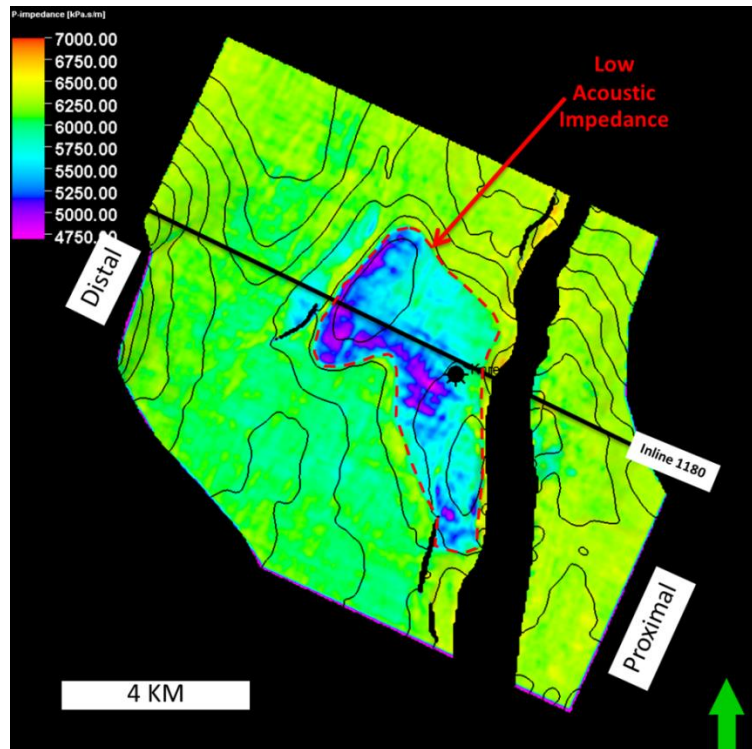


Figure 6-29: The distribution of acoustic impedance on H-4 surface. Search window (below or above H-4) was zero ms TWT. The green arrow indicates the north direction.

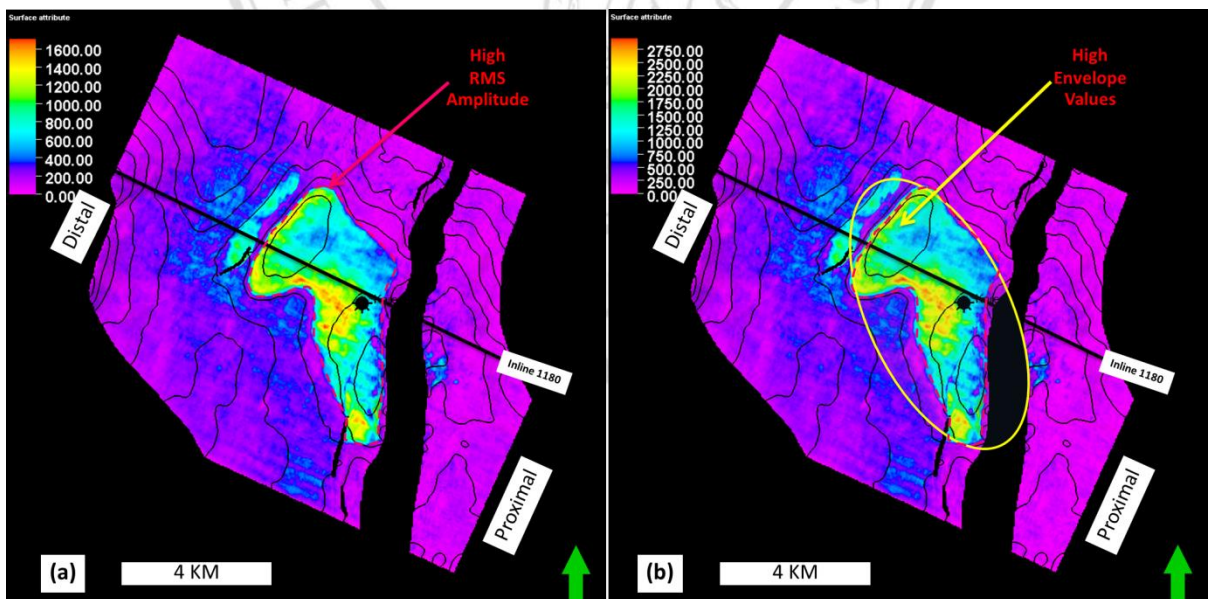


Figure 6-30: (a) RMS amplitude attribute map of H-4, and (b) Envelope attribute map of H-4. Search window (below or above H-4) was zero ms TWT. The green arrow indicates the north direction.

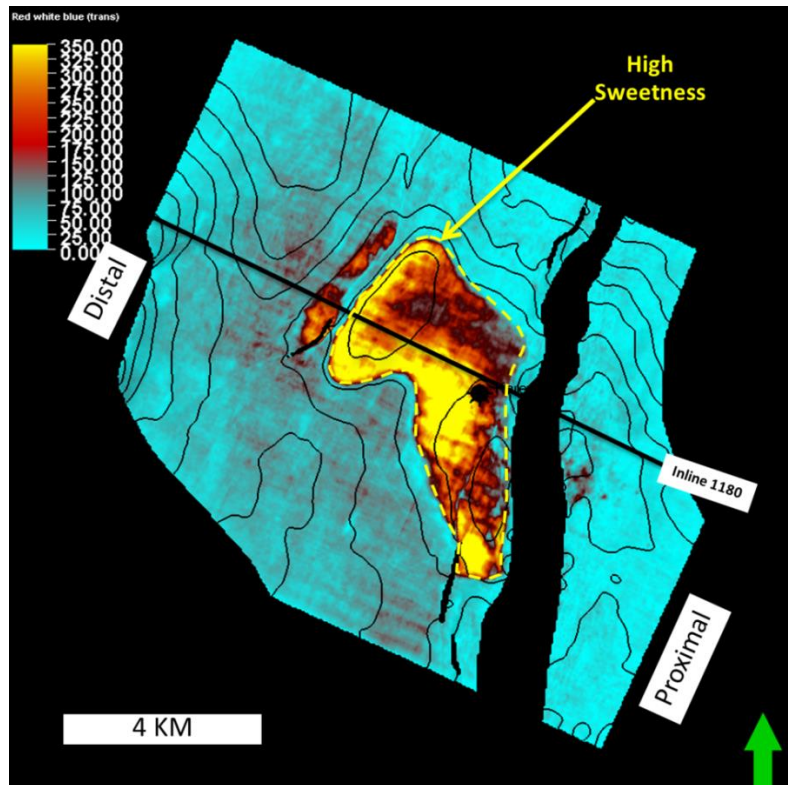


Figure 6-31: Sweetness attribute map of H-4. Search window (below or above H-4) was zero ms TWT. The green arrow indicates the north direction.

H-5 (Intra Mangaa C-1) was interpreted on a positive amplitude reflection (peak) of high continuity (section 5.1). The acoustic impedance distribution map of H-5 (Figure 6-32) ranges from 5700 to 7000 ((m/s)*(g/cc)) and shows that H-5 has medium to high range of acoustic impedance in most of its area except in the NW. In the NW area there is comparatively medium acoustic impedance ranging from 5700 to 6300 ((m/s)*(g/cc)). This difference can be occurred due to the lithology variation, and comparatively low amplitude reflections.

In Figure 6-33, the RMS amplitude and envelope attribute map of H-5 shows the high RMS amplitude and high envelope values at the same zone whereas the acoustic impedance distribution map shows low acoustic impedance. The sweetness distribution map of H-5 is shown in Figure 6-34. It shows the high sweetness values at the same zone whereas the RMS amplitude and envelope map showed high values.

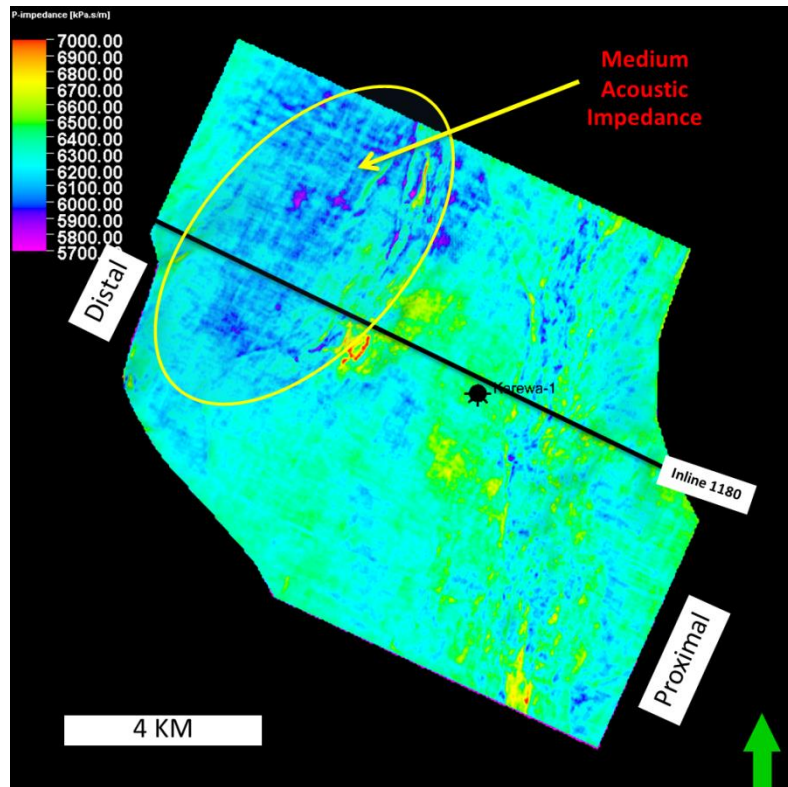


Figure 6-32: The distribution of acoustic impedance on H-5 surface. Search window (below or above H-5) was zero ms TWT. The green arrow indicates the north direction.

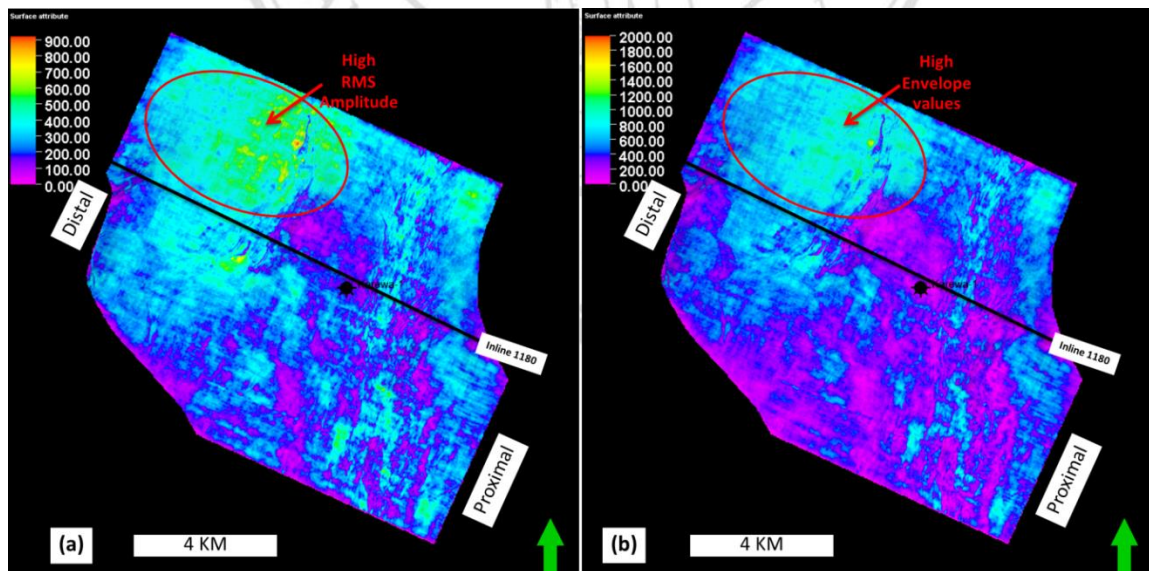


Figure 6-33: (a) RMS amplitude attribute map of H-5, and (b) Envelope attribute map of H-5. Search window (below or above H-5) was zero ms TWT. The green arrow indicates the north direction.

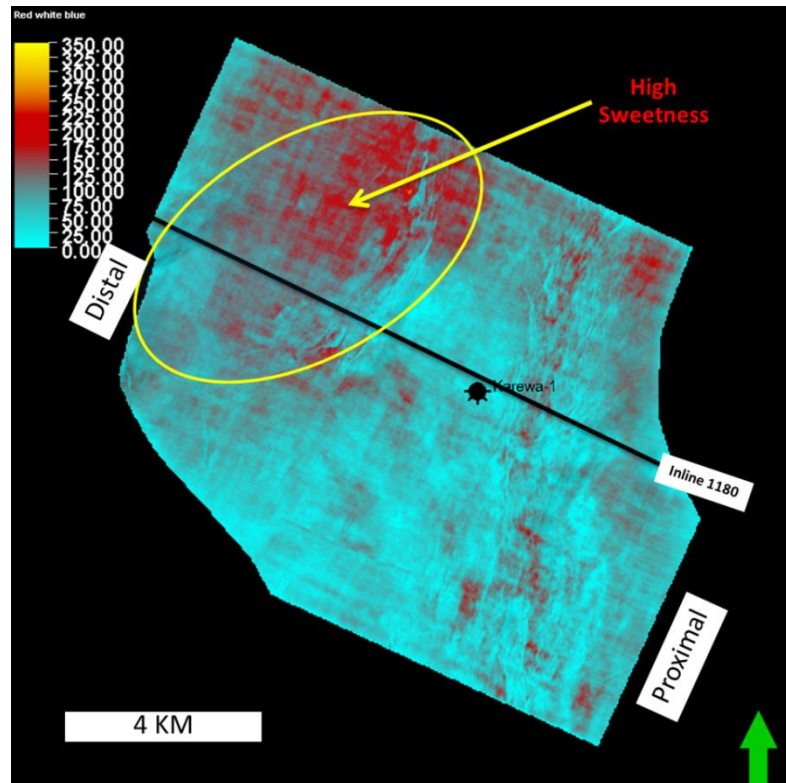


Figure 6-34: Sweetness attribute map of H-5. Search window (below or above H-5) was zero ms TWT. The green arrow indicates the north direction.

H-6 (2191ms TWT at the Karewa-1 well location in inline 1178) was interpreted on a prominent positive amplitude reflection (peak) of medium continuity (chapter 5, section 5.1). The acoustic impedance distribution map of H-6 (Figure 6-35) ranges from 5800 to 8000 ((m/s)*(g/cc)). It shows that H-6 has high range of acoustic impedance in north and NE which ranges from 7000 to 8000 ((m/s)*(g/cc)). On the other hand, medium to high acoustic impedance distribution is found in the south and SW which ranges from 5800 to 8000 ((m/s)*(g/cc)). This difference might be occurred due to the lithology variations and high variation of depth of H6 (section 5.1).

In Figure 6-36, the RMS amplitude and envelope attribute map of H-6 shows the medium to high values in the south and SW and comparatively low values in the north and NE. The acoustic impedance variation or contrast in the south and SW is observed in better way because of the high values of amplitude. The sweetness attribute map of H- is shown in Figure 6-37. It shows the high sweetness values at the same zone where the high values of RMS amplitude and envelope is found.

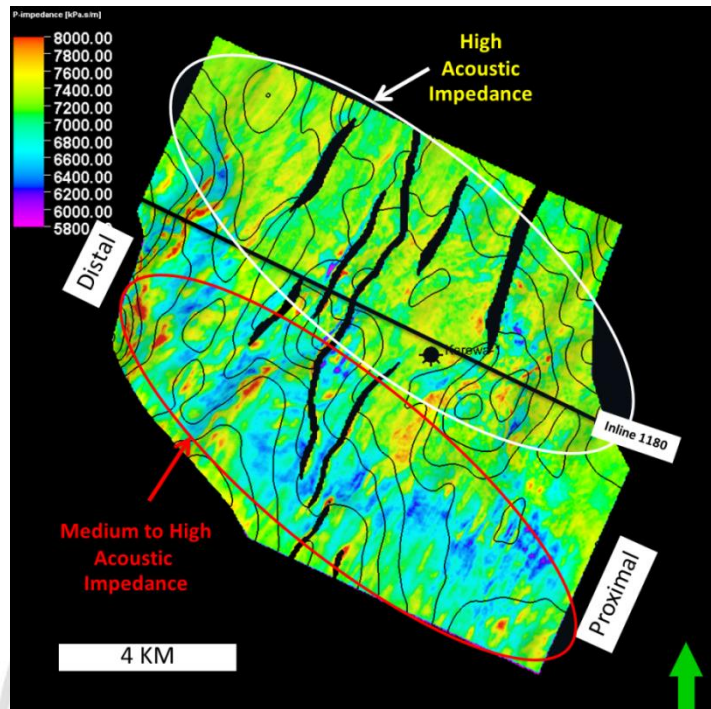


Figure 6-35: The distribution of acoustic impedance on H-6 surface. Search window (below or above H-6) was zero ms TWT. The green arrow indicates the north direction.

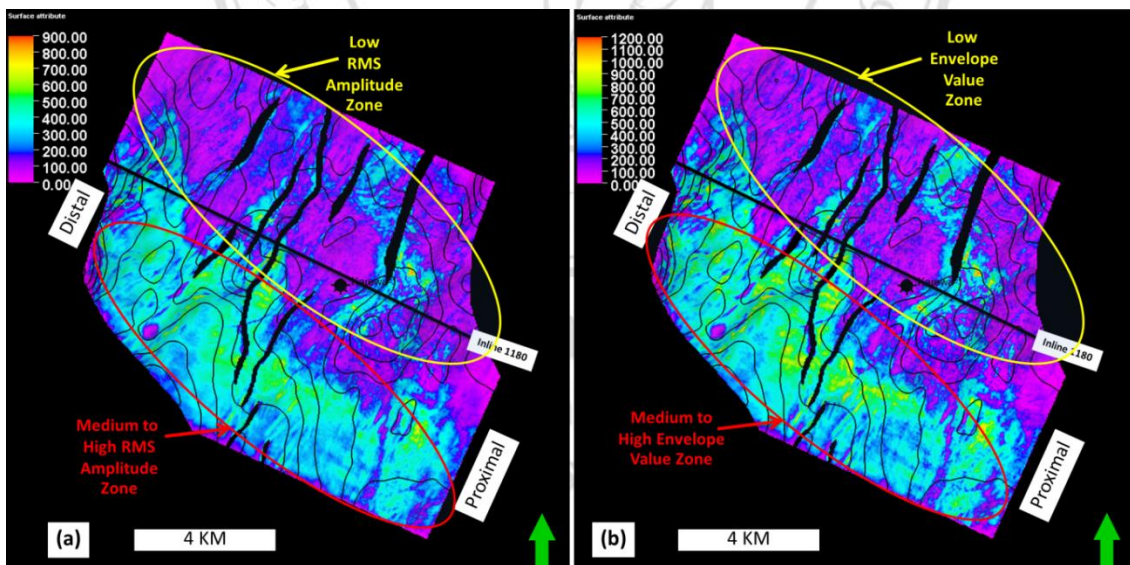


Figure 6-36: (a) RMS amplitude attribute map of H-6, and (b) Envelope attribute map of H-6. Search window (below or above H-6) was zero ms TWT. The green arrow indicates the north direction.

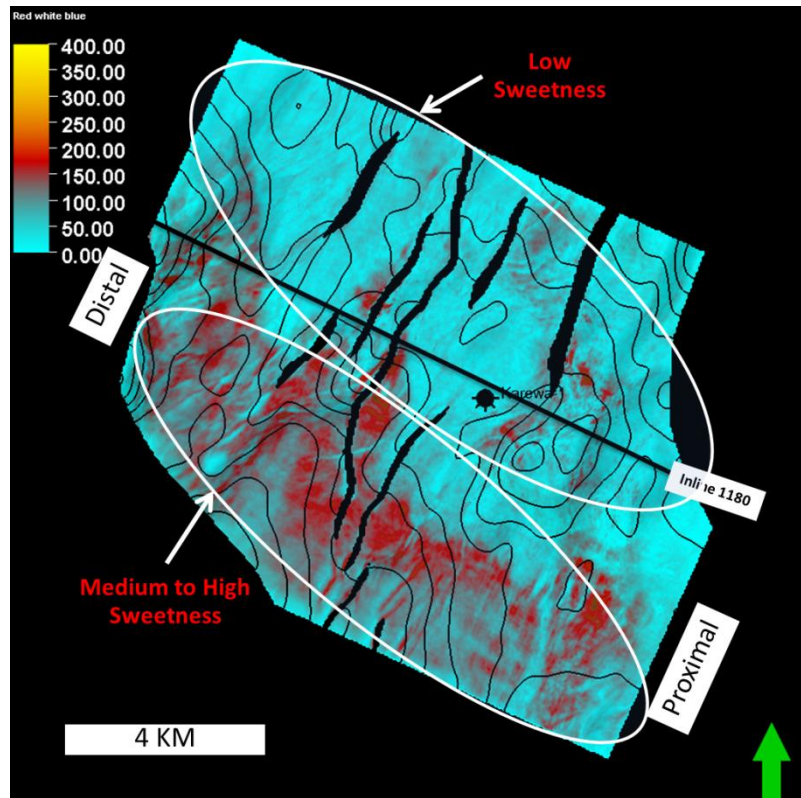


Figure 6-37: Sweetness attribute map of H-6. Search window (below or above H-6) was zero ms TWT. The green arrow indicates the north direction.

ลิขสิทธิ์มหาวิทยาลัยเชียงใหม่
 Copyright© by Chiang Mai University
 All rights reserved